AGU PUBLICATIONS

JGR

Journal of Geophysical Research: Oceans

RESEARCH ARTICLE

10.1002/2015JC010739

M_2 baroclinic tide variability modulated by the ocean circulation south of Japan

Sergey M. Varlamov[1], Xinyu Guo[1,2], Toru Miyama[1], Kaoru Ichikawa[3], Takuji Waseda[1,4], and Yasumasa Miyazawa[1]

[1]Application Laboratory, Japan Agency for Marine-Earth Science and Technology, Yokohama, Japan, [2]Center for Marine Environmental Studies, Ehime University, Matsuyama, Japan, [3]Research Institute for Applied Mechanics, Kyushu University, Kasuga, Japan, [4]Graduate School of Frontier Science, University of Tokyo, Kashiwa, Japan

Key Points:
- Concurrent simulation of tide and ocean circulation in the North Western Pacific
- Modulation of M_2 baroclinic tide by ocean circulation
- Energy cycle analysis of baroclinic tide

Correspondence to:
Y. Miyazawa,
miyazawa@jamstec.go.jp

Citation:
Varlamov, S. M., X. Guo, T. Miyama, K. Ichikawa, T. Waseda, and Y. Miyazawa (2015), M_2 baroclinic tide variability modulated by the ocean circulation south of Japan, *J. Geophys. Res. Oceans*, *120*, 3681–3710, doi:10.1002/2015JC010739.

Received 20 JAN 2015
Accepted 13 APR 2015
Accepted article online 25 APR 2015
Published online 25 MAY 2015

Abstract We analyze a concurrent simulation result of the ocean circulation and tidal currents using a data-assimilative ocean general circulation model covering the Western North Pacific with horizontal resolution of 1/36° to investigate possible interactions between them. Four sites of active M_2 internal tide variability in open ocean (hot spots), such as Tokara Strait, Izu Ridge, Luzon Strait, and Ogasawara Ridge, are detected from both the satellite observation and the simulation. Energy cycle analysis of the simulated M_2 baroclinic tide indicates two types of the hot spots: dissipation (Tokara Strait and Izu Ridge) and radiation (Luzon Strait and Ogasawara Ridge) dominant sites. Energy conversion from barotropic to baroclinic M_2 tides at the hot spots is modulated considerably by the lower-frequency changes in the density field. Modulation at the two spots (Tokara Strait and Izu Ridge) is affected by the Kuroshio path variation together with the seasonal variation of the shallow thermocline. At the other two sites, influence from changes in the relatively deep stratification through the Kuroshio intrusion into South China Sea (Luzon Strat) and mesoscale eddy activity (Ogasawara Ridge) is dominant in the modulation.

1. Introduction

The baroclinic (internal) tides, which involve vertical oscillations of the isopycnal surfaces, are activated by the interaction between the barotropic (external) tide and bottom topography [*Cox and Sandstrom*, 1962; *Baines*, 1973; *Wunsch*, 1975; *Kantha and Tiereney*, 1997]. They play a key role in dissipation of the barotropic tides and mixing in the deep layer through their wave breaking and dissipation [*Munk and Wunsh*, 1998; *Qiu et al*., 2012]. The satellite altimetry analysis reveals the wide distribution of the baroclinic tide by focusing on the stationary periodic (coherent) sea level variations with M_2 semidiurnal tidal frequency [*Ray and Mitchum*, 1996]. Some studies based on the field observations suggest active interactions between the baroclinic tides and lower-frequency phenomena, which result in the time-dependent (incoherent) nature of the baroclinic tide. The incoherence of the baroclinic tides is caused by their modulation through the variations in the background stratification and the changes of the phase speed caused by the ambient flows [*Eich et al*., 2004; *Chavanne et al*., 2010; *Zilverman et al*., 2011].

Recent development of the ocean modeling includes concurrent simulations of tides and lower-frequency ocean circulations in global [*Arbic et al*., 2010, 2012] and regional [*Kartadikaria et al*., 2011; *Osborne et al*., 2011; *Jan et al*., 2012; *Kerry et al*., 2014] scales. Those results demonstrate that the baroclinic tide variability is affected by the spatiotemporally varying stratification and ambient currents and it modifies the mesoscale water mass structures.

Motivated by such simulation studies, using a state of art tide-resolving ocean general circulation model: JCOPE-T, we examine the incoherence of the baroclinic tide variability south of Japan where both the baroclinic tide [*Niwa and Hibiya*, 2001, 2004, 2011] and mesoscale eddy [*Pascual et al*., 2006] variations are very active. JCOPE-T is operationally utilized for the ocean state prediction at Japan Agency for Marine-Earth Sciences and Technology (JAMSTEC), and the visualization of the real-time prediction based on the latest version of JCOPE-T is available from the website: http://www.jamstec.go.jp/jcope/vwp/. This model demonstrates some skills representing the complicated ocean current variations associated with the interactions among the wind-driven, tidal, river discharge, and open ocean currents [*Miyazawa et al*., 2012, 2013].

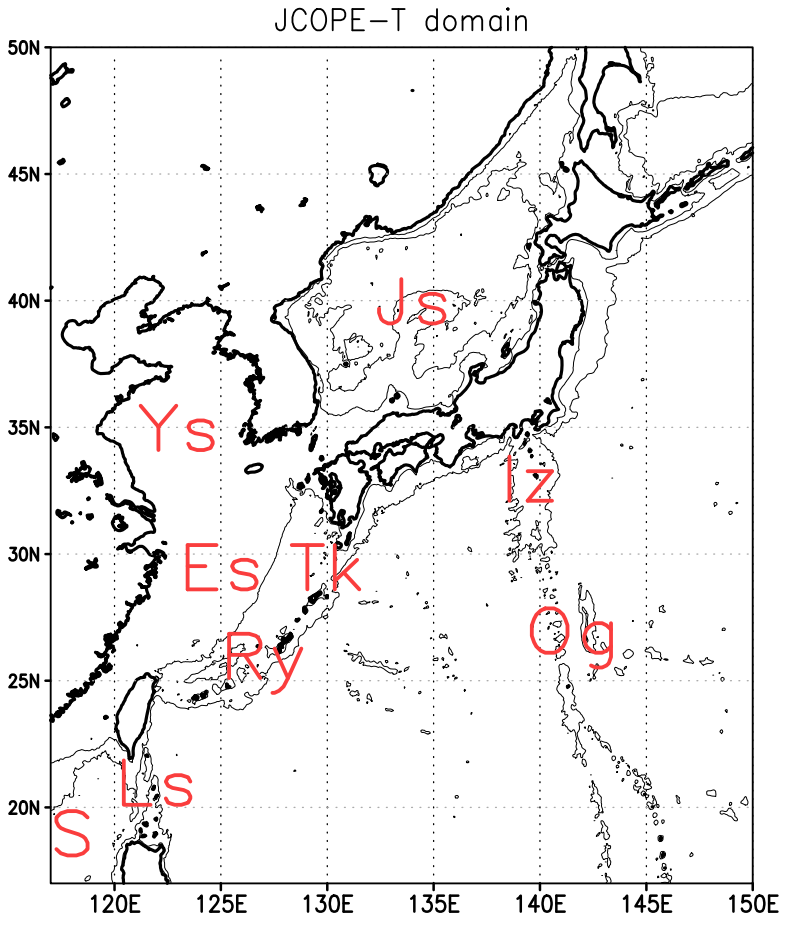

Figure 1. Topography of the JCOPE-T model domain. Thick (thin) contours denote shorelines (isodepth line with 200 and 2000 m). The abbreviations represents locations (S, South China Sea; Ls, Luzon Strait; Ry, Ryukyu Islands Chain; Og, Ogasawara Ridge; Es, East China Sea; Tk, Tokara Strait; Iz, Izu Ridge; Ys, Yellow Sea; and Js, Japan Sea).

We focus on the modulation of the baroclinic tide energetics in some areas of their active generation by the lower-frequency ocean circulation processes, which topic has not been fully investigated until now. The previous studies analyzing the baroclinic tide energetics in the Western North Pacific did not include the ocean general circulation dynamics in their simulations [*Niwa and Hibiya*, 2001, 2004, 2011; *Kerry et al*., 2013]. A few studies recently showed that the presence of Kuroshio and/or mesoscale eddies [e.g., *Jan et al*., 2012; *Kerry et al*., 2014] modulate both the generation and propagation of the baroclinic tidal energy under some idealized situations. In this study, we elucidate the temporal dependence of the M_2 baroclinic tide energy budget in active generation sites of the baroclinic tide south of Japan on the spatiotemporal changes in the background stratification, which are driven by the lower-frequency ocean general circulation processes including the Kuroshio and mesoscale eddies representing the realistic behaviors allowed by the data assimilation.

This paper is organized as follows. Section 2 provides a description on the tide-resolving, operational ocean general circulation model for the Western North Pacific, JCOPE-T, and reports the validation of the M_2 baroclinic tide using the Jason-2 satellite altimeter data. Section 3 describes the M_2 baroclinic tide energetics using the simulation data from sensitivity experiment simulations designed for investigation of the modulation of M_2 baroclinic tide. The incoherent M_2 baroclinic tide variability induced by changes in the background stratification is discussed in section 4. The final section is devoted to summary. Appendices describe the tidal forcing scheme of our model (Appendix A) and the validation of the simulated M_2 tide using the Jason-2 data, a barotropic tide model used for providing the tidal forcing of our model, and the tide gauge data (Appendix B).

2. Tide-Resolving Ocean Circulation Simulation

We conducted a 1 year reanalysis simulation using a tide-resolving general circulation model (JCOPE-T) that was developed based on the Princeton Ocean Model with a general coordinate of sigma (POMgcs) [*Mellor et al*., 2002]. JCOPE-T has a horizontal resolution of 1/36° and 46 generalized sigma layers and covers a part of the Western North Pacific: 17°N–50°N and 117°E–150°E (Figure 1) nested in an outer model, JCOPE2 [*Miyazawa et al*., 2009]. Note that another version of JCOPE-T covering a smaller region: 28°N–44°N, and 125°E–

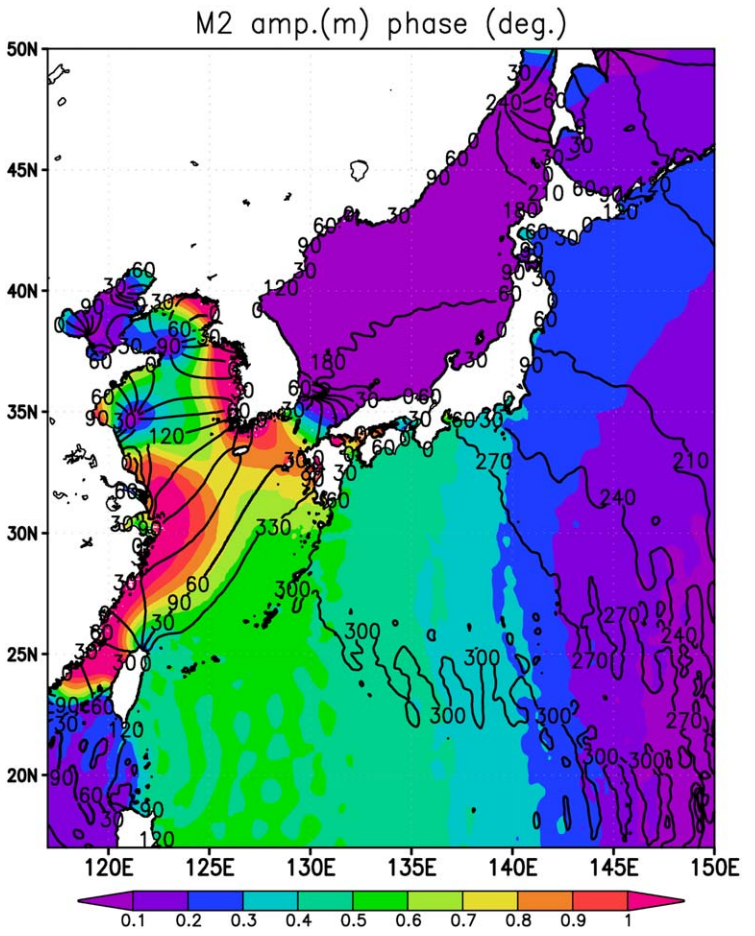

Figure 2. Amplitude (in m) of M_2 surface tidal elevation in the JCOPE-T simulation. Black lines denote lines of constant phase with 30° interval.

148°E has been used for the investigation of the radionuclide dispersion around Japan [*Miyazawa et al.*, 2012, 2013]. The outer model (JCOPE2) with no-tide provides the daily mean information on the open boundary of JCOPE-T using a one-way nesting technique [*Guo et al.*, 2003; also see Appendix A].

We modify the original POMgcs to implement a fourth order baroclinic pressure gradient scheme [*McCalpin*, 1994; *Berntsen and Oey*, 2010] and a flux-corrected transport scheme for tracer advection [*Boris and Book*, 1973] instead of the second order pressure gradient and the central difference advection schemes, respectively. In addition, we include the lateral horizontal diffusion along not a sigma-level but along a z-level to avoid formation of erroneous temperature and salinity values near the steep bottom topography. The horizontal viscosity coefficient for the harmonic schemes is evaluated using the *Smagorinsky's* [1963] formula with a constant of 0.3, and horizontal diffusion coefficient is fixed as 50 $m^2 s^{-1}$. The vertical viscosity and diffusion processes are also described by the harmonic schemes with the coefficients calculated using the Mellor-Yamada's level 2.5 turbulent closure model [*Mellor and Yamada*, 1982] modified by the inclusion of the surface wave breaking effects [*Mellor and Blumberg*, 2004]. The usual bottom stress scheme originally included in the Princeton Ocean Model [see *Mellor*, 2002, equation (14)] effectively works for reasonable representation of the bottom friction except for biases to the observed sea level amplitude of the tide in some part of the nearshore region (Appendix B).

The model is driven by the surface momentum, heat, and freshwater fluxes calculated by an algorithm proposed by *Li et al.* [2010] with use of modeled sea surface temperature and hourly atmospheric data provided from National Centers for Environmental Prediction Global Forecast System (NCEP GFS) as 6 h analyses and hourly forecasts. Details of the tidal forcing are described in Appendix A. Lateral freshwater inputs from 47 major Japanese rivers, 3 rivers on the Korean Peninsular, 1 Taiwan river, and 7 Chinese main land rivers are accounted by JCOPE-T. Monthly mean volume fluxes of the river discharges [*Ministry of Land, Infrastructure, Transport, and Tourism*, 2002; *Wang et al.*, 2008; see the Global River Discharge Database, http://www.sage.wisc.edu/riverdata/] are specified for the grid boxes corresponding to the river mouths. River water is assumed to have zero salt content and temperature equal to maximum of air temperature or water freezing temperature (0°C). Inflow is going to upper model layers corresponding to river mouth depth (default 5 m).

Observed features of geostrophic phenomena including the Kuroshio and mesoscale eddies are involved in JCOPE-T through a nudging of temperature and salinity fields to those provided by the data-assimilative

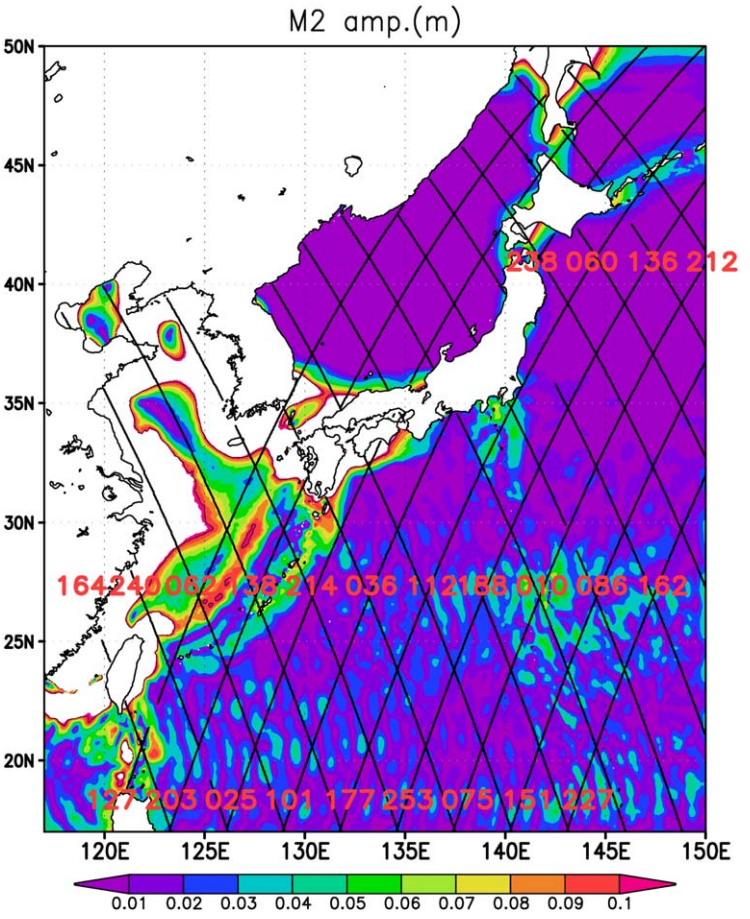

Figure 3. Amplitude (in m) of M_2 surface tidal elevation evaluated from the high-pass filtered sea surface height anomaly of the JCOPE-T simulation. The amplitude larger than 0.109 m is excluded from the shading. Black lines denote the Jason-2 satellite altimeter tracks. Numerics with three digits indicate the pass numbers.

JCOPE2 model [*Miyazawa et al.*, 2009] with the relaxation time scale of 5 day [*Miyazawa et al.*, 2013]. The JCOPE2 model, which represents no tidal current, assimilates the detided sea surface height anomaly obtained from the satellite altimetry, satellite sea surface temperature, and in situ temperature and salinity profiles [*Miyazawa et al.*, 2009]. To avoid suppressing the high-frequency variability including tide, we add the nudging term proportional to the difference between the 5 day running mean values of JCOPE-T and the daily mean values of JCOPE2 interpolated on the JCOPE-T grids to the original temperature and salinity equations, which could be considered as a variant of the spectral nudging methods [e.g., *Waldron et al.*, 1996]. The model was initialized with the flow, temperature and salinity interpolated from JCOPE2 on 1 December 2010. Hourly results of sea level, current, temperature, and salinity of JCOPE-T for a period from 1 March 2011 to 1 March 2012 are used for analyses.

A corange and cophase map of the M_2 tidal constituent of the simulated SSHA (Figure 2) shows the westward propagation of the M_2 tidal wave from the central part of the Western North Pacific, and increase (decrease) of the amplitude in the marginal seas including the East China, and Yellow Seas (Japan Sea). Those features are similar to the previous results of barotropic and baroclinic tides simulations [*Egbert et al.*, 1994; *Guo and Yanagi*, 1998; *Niwa and Hibiya*, 2001]. In addition, O (100 km) short wavelength fluctuations in both amplitude and phase are apparent in South China Sea and east of Taiwan. These are related to the baroclinic tide variability [*Niwa and Hibiya*, 2001; *Arbic et al.*, 2012]. Detailed comparison of the simulated M_2 tide with that evaluated from the satellite altimetry (Jason-2), from the barotropic tide model used for the tidal forcing at the open boundaries, and from the tide gauge data is described in Appendix B.

The surface manifestation of the baroclinic tide is detected by a high-pass filter of SSHA [*Ray and Mitchum*, 1996; *Matsumoto et al.*, 2000; *Niwa and Hibiya*, 2001]. Figure 3 depicts the amplitude of M_2 harmonic constituent evaluated from the high-pass filtered SSHA of the simulation. We set cutoff scale of 200 km of the Gaussian filter based on the consideration on a typical wavelength of 110 km for the semidiurnal baroclinic tide assuming a first mode baroclinic wave speed of 2.5 m/s [*Kantha and Tierney*, 1997]. The distribution of smaller spatial scale M_2 amplitude indicates localized intense variability around the steep topographic slopes in the Western North Pacific including Ryukyu Islands Chain, Tokara Strait, Izu and Ogasawara Ridges, and Luzon Strait (see Figure 1 for locations). The M_2 amplitude estimated from the variation of 26.7 Sigma-t isopycnal surface also shows the similar patterns (not shown), suggesting that the high-pass filtering of the

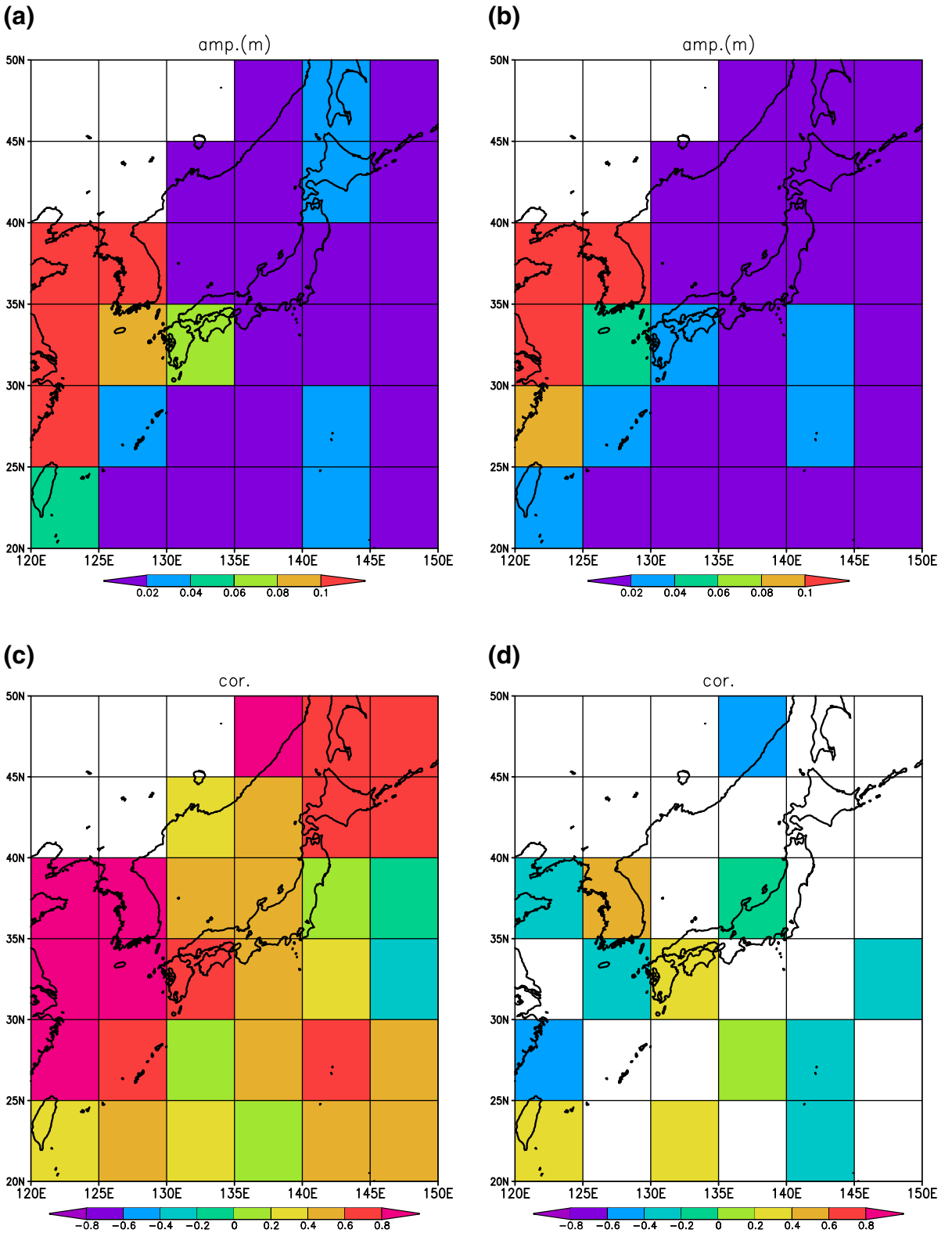

Figure 4. (a) M_2 tidal amplitudes (in m) evaluated from the high-pass filtered sea surface height anomaly along the Jason-2 tracks averaged in square regions of 5° by 5°. (b) As in Figure 4a except for the JCOPE-T simulation data. (c) Correlation between the M_2 tidal amplitude of the Jason-2 observation and JCOPE-T simulation evaluated from the high-pass filtered sea surface height anomaly along the Jason-2 tracks within square regions of 5° by 5°. Statistically insignificant regions are excluded from the shading. (d) As in Figure 4c except for phase.

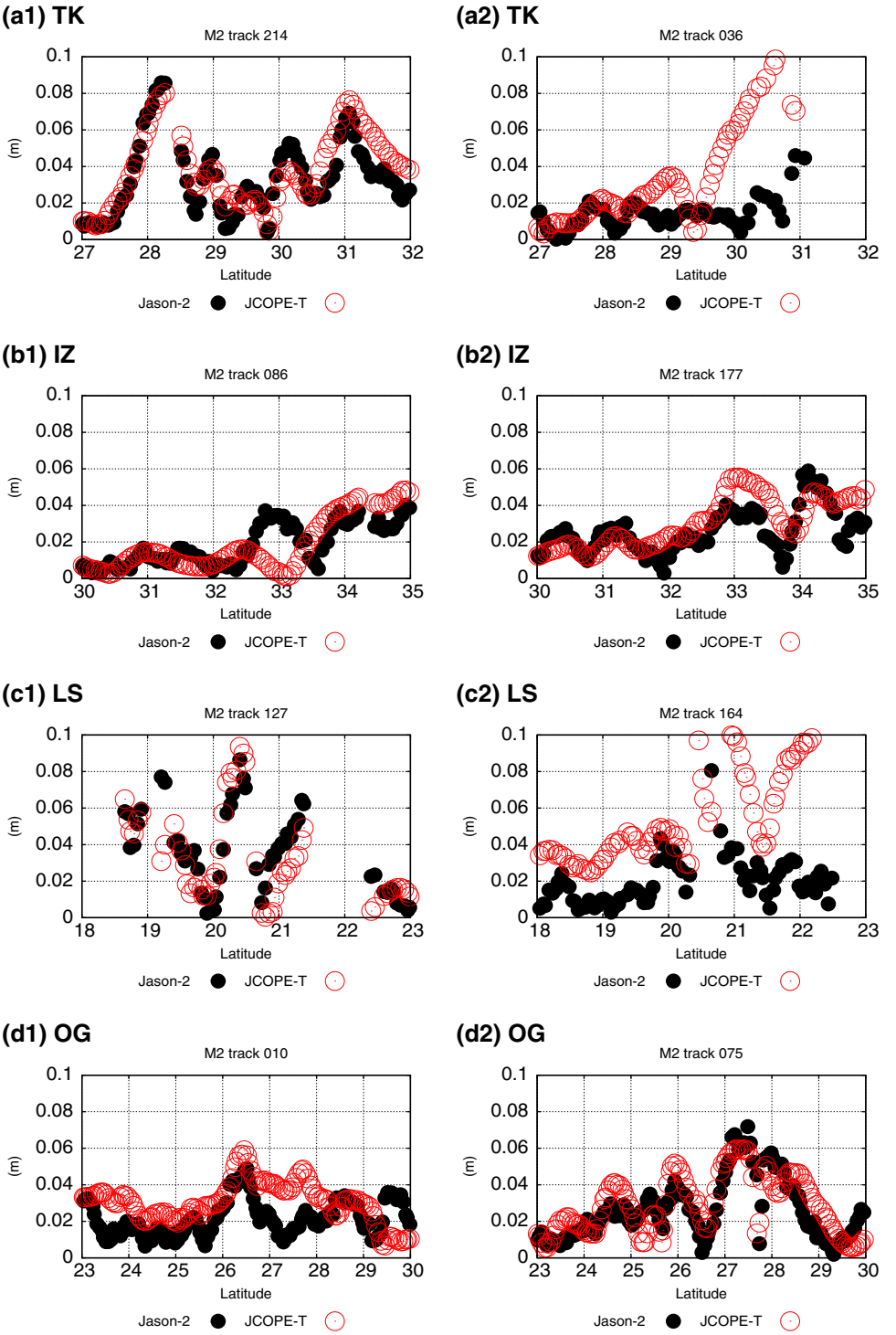

Figure 5. M_2 tidal amplitude from the high-pass filter sea surface height anomaly along the Jason-2 satellite altimeter tracks. Closed (open) circles denote the JCOPE-T simulation (the Jason-2 observation). Around (a) Tokara Strait, (b) Izu Ridge, (c) Luzon Strait, and (d) Ogasawara Ridge.

simulated SSHA is an effective way for detection of the M_2 baroclinic tide variability. Note that the simulation shows comparatively larger amplitude in East China Sea and Yellow Sea.

The M_2 amplitude distributions of the satellite observed (Appendix B) and simulated high-pass filtered SSHA also exhibit good agreement with each other, and both demonstrate a smaller magnitude (Figures 4a

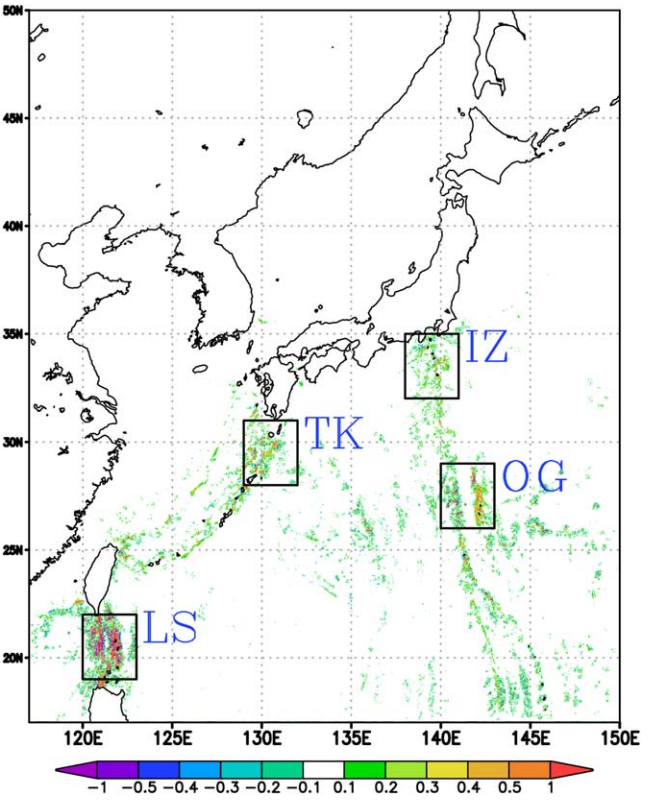

Figure 6. Depth-integrated BEC rate (in W m^{-2}) evaluated from the "M_2-Tide" simulation. Boxes indicate the regions of the active generation sites of the baroclinic tides (hot spots): Tokara Strait, Izu Ridge, Luzon Strait, and Ogasawara Ridge (see Figure 1 for locations).

and 4b) as compared to those of the nonfiltered SSHA (Figures A1a and A1b). A correlation map for the amplitude (Figure 4c) indicates that the simulation has a skill representing the observed amplitude distributions; however, it basically fails to reproduce the observed phase distribution (Figure 4d). The relatively simple spatial filter used in the present study might be sensitive to noises included in the phase information.

The distribution of the M_2 amplitude estimated from the high-pass filtered SSHA (Figure 3) represents the localized intense variability (hot spots) in the Western North Pacific. Comparison of the observed and simulated M_2 amplitudes along the tracks (Figure 3) around some hot spots: Tokara Strait, Izu Ridge, Ogasawara Ridge, and Luzon Strait (for locations, see Figures 1 and 5) suggests that the simulation generally represents the amplitudes around there as observed though it tends to slightly overestimate them in shallower part of the model region (Figures 5a2 and 5c2; also see Figure 3).

3. M_2 Baroclinic Tidal Energetics

The M_2 baroclinic tide variability can be investigated quantitatively based on the analysis of its energy transformations. We suppose a governing equation for the depth-integrated baroclinic energy as follows [*Niwa and Hibiya*, 2004]:

$$\frac{\partial E_{bc} D}{\partial t} = -\left(\frac{\partial \overline{P' U'} D}{\partial x} + \frac{\partial \overline{P' V'} D}{\partial y}\right) + g\overline{\rho' w'_{bt}} D + \overline{DIS_{bc}} + \overline{ADV_{bc}}, \tag{1}$$

where the primed variables are the baroclinic components that are defined as the deviation from the vertical mean values, the overbar denotes the average over the entire water column, E_{bc} is the baroclinic energy density, P' is the pressure perturbation associated with the density variation, and w_{bt} is the Cartesian vertical velocity associated with the barotropic flow given by

$$w_{bt} = \overline{U}\left(\sigma\frac{\partial D}{\partial x} + \frac{\partial \eta}{\partial x}\right) + \overline{V}\left(\sigma\frac{\partial D}{\partial y} + \frac{\partial \eta}{\partial y}\right) + (\sigma+1)\frac{\partial \eta}{\partial t}, \tag{2}$$

where D, (U, V), σ, and η are the bottom depth, horizontal velocity, sigma-level, and sea surface height, respectively, and DIS_{bc} and ADV_{bc} denote the dissipation and advection, respectively. Integrating equation (1) over a fixed area and averaging over one tidal period (denoted by an angle bracket) lead to the conservation equation for the baroclinic energy [*Niwa and Hibiya*, 2004; *Lorenzo et al.*, 2006],

$$\iint_S \langle g\overline{\rho' w_{bt}} D\rangle ds \cong \int_C \langle \overline{P' U'}_n D\rangle dl - \left(\iint_S \langle \overline{DIS_{bc}}\rangle ds + \iint_S \langle \overline{ADV_{bc}}\rangle ds\right), \tag{3}$$

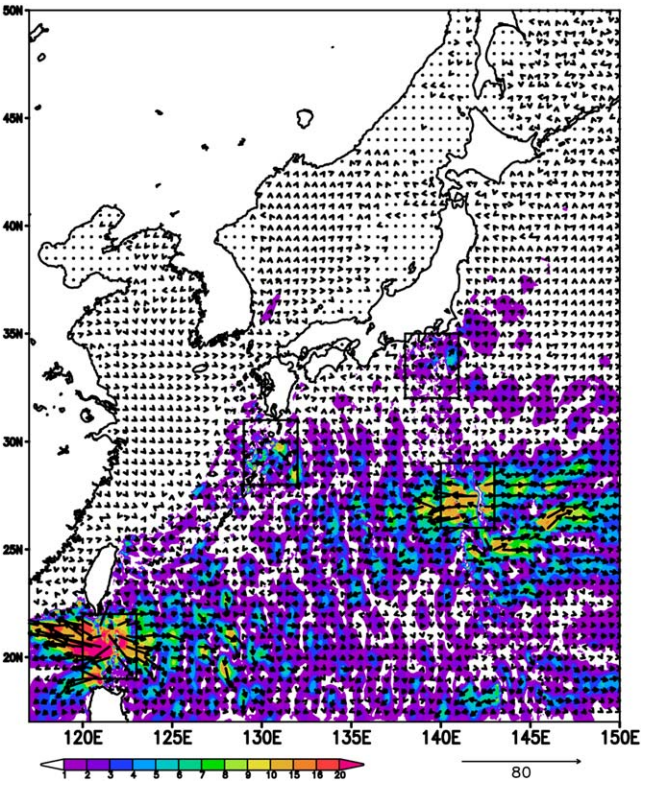

Figure 7. As in Figure 6 except for magnitude of the M_2 baroclinic energy radiation flux (in kW m^{-1}). Vectors indicate the direction and magnitude.

where U_n denotes the velocity outward normal to the boundary of area C, ds is an infinitesimal element of the area S, and dl is an infinitesimal element along the boundary C. The term of the left-hand side of equation (3) specifies the total energy of baroclinic tide generated through the tidal barotropic to baroclinic energy conversion (BEC). The first term of the right-hand side of equation (3) indicates a part of the total energy radiated from the boundary of area C. The remaining part of the energy is locally advected and dissipated inside of the area S as represented by the second term of the right-hand side of equation (3).

To investigate the simulated M_2 baroclinic tide energetics in detail, we conducted two additional simulations forced by the tidal forcing with the M_2 constituent alone, which allow a relatively short harmonic analysis period owing to no need of extracting the M_2 signal from the simulated variations forced by the similar frequency tidal constituents. For these experiments, our choice of the harmonic analysis period is 3 days that is long sufficient to distinguish the M_2 and inertial motions in the model region. One additional simulation case ("M_2-Tide") is almost same as the original simulation with realistic multi-constituents tide except that tide is limited by a M_2 constituent alone. Another simulation ("Only M_2-tide") is performed with an initially horizontally uniform temperature and salinity distribution for the whole domain, forced by only the M_2 tide with zero surface momentum, heat and freshwater fluxes and zero lateral boundary nontidal flow. This experiment excludes impacts of variable stratification forced by no-tidal processes including mixed layer variation, and geostrophic and wind-driven currents on tidal processes though it still allows generation of internal tidal waves and corresponding energy conversion. This experiment is run for a period from 10 December 2010 to 22 March 2012. Initial vertical temperature and salinity profiles are evaluated using the World Ocean Atlas 2001 climatology data [*Conkright et al.*, 2002].

For the case "M2-Tide," we examine the time evolution of the M_2 tidal energetics by running harmonic analysis for sea surface height, current, and density for different 182 consecutive subperiods with 3 days duration during the 1 year simulation period. Each subperiod overlaps 1 day with the former and succeeding subperiods. The first subperiod begins from 1 March 2011 and the last one begins from 26 February 2012. We also evaluate the harmonics of the case "Only M_2-Tide" for different 25 subperiods with the first subperiod beginning from 1 January 2011 and the last one beginning from 14 March 2011. Note that the energy budget analysis evaluated from the base simulation forced by a multiple tidal constituents, which requires longer harmonic analysis duration of at least 30 days for distinguishing M_2 and S_2 signals, shows basically similar results to those discussed below (not shown).

Figure 6 shows the M_2 BEC averaged for all subperiods of the case "M_2-Tide." The energy conversion is active around the steep bottom topography including Tokara Strait, Izu-Ogasawara Ridges, and Luzon Strait indicated by squares in Figure 6, and the distribution is partly similar to that of the amplitude of M_2 harmonic constituent evaluated from the high-pass filtered SSHA (Figure 3).

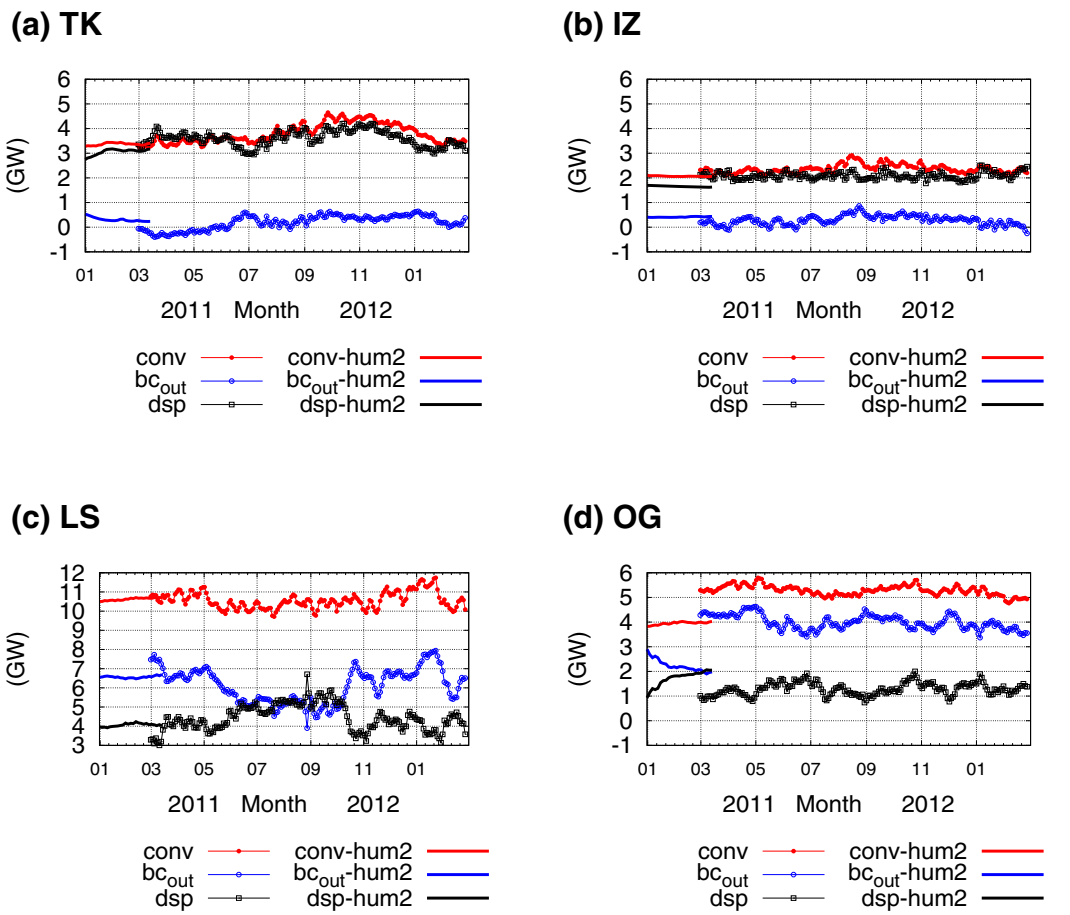

Figure 8. M_2 baroclinic tidal energy budgets (see equation (3)) calculated at the hot spots (see Figures 1 and 7 for their locations and areas, respectively) for the subperiods with 3 day duration (see the text for the definition). Closed circles: BEC. Open circles: the divergence of the energy radiation fluxes. Open squares: the dissipation and advection.

A distribution of the energy radiation flux of the M_2 baroclinic tide $\left(\langle \overline{P'U'}D\rangle, \langle \overline{P'V'}D\rangle\right)$ averaged for the all subperiods (Figure 7) represents that the four hot spots intensively radiate the M_2 baroclinic tide energy. Magnitudes of the radiation depend on those of the energy conversion (Figure 6), showing relatively smaller magnitudes of the radiation in both of Tokara Strait and Izu Ridge as compared to more active radiation around the Ogasawara Ridge and Luzon Strait. Streaks patterns shown between the ridges at west and east sides are similar to those shown in the high-pass filtered M_2 signal (Figure 3), suggesting the possible remote effects due to the wave propagation [*Kerry et al.*, 2013] together with the intensification of the energy generation caused by the local sea mountains.

Time sequences of the energy budget equation (3) at the four hot spots for the all subperiods are shown in Figure 8 (also see mean and standard deviation for the all subperiods described in Table 1). BEC rates and contribution from the radiation in the two hot spots (Tokara Strait and Izu Ridge) are relatively smaller than those in the other two spots (Ogasawara Ridge and Luzon Strait). The situation is reverse for the local dissipation and advection term that is larger in the former two spots than that in the latter two spots. Figure 8 shows the results from both the cases of "M_2-Tide" and "Only M_2-Tide." The case with only the M_2 tide

Table 1. Mean and Standard Deviation (in Parentheses) During the 1 Year Simulation Period of the "M_2-Tide" Simulation of BEC Rates Averaged at the Spots and the Depth-Integrated Tidal Energy Supply Into the Spots

(GW)	Tokara Strait	Izu Ridge	Luzon Strait	Ogasawara Ridge
BEC	3.80 (0.39)	2.37 (0.17)	10.56 (0.43)	5.28 (0.20)
Supply	46.45 (1.29)	36.47 (0.80)	58.27 (1.86)	33.32 (0.78)

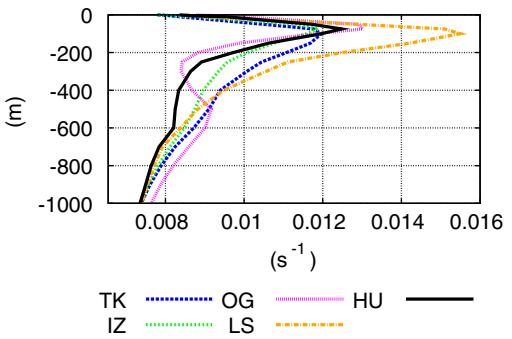

Figure 9. Time-mean horizontally averaged vertical profiles of the buoyancy frequency at the spots: TK, Tokara Strait; IZ, Izu Ridge; LS, Luzon Strait; and OG, Ogasawara Ridge, calculated from the "M_2-Tide" simulation result. A profile "HU" denotes a climatological mean profile calculated from World Ocean Atlas 2001 [*Conkright et al.*, 2002] and it is used for the "Only M_2-Tide" simulation.

forcing, "Only M_2-Tide," results in almost stationary BEC values after some initial adjustment in the all spots. Driven by a periodic M_2 forcing alone, the subtidal state of the model slowly evolves together with changing stratification. Stratification change is caused by tide-induced mixing generated by vertical shear of tidal currents. Magnitude of each term is generally similar between "Only M_2-Tide" and "M_2-Tide" except for Ogasawara Ridge (Figure 8d) showing considerably smaller (larger) conversion and radiation (dissipation and advection) in "Only M_2-Tide" than in "M_2-Tide." This arises from the difference in the vertical profiles of the mean stratification used in these simulations; the vertical density profile used in "Only M_2-Tide" does not show a local maximum around 500 m depth at Ogasawara Ridge, while it is clearly represented in the mean profile in "Tide-M_2" case (Figure 9). This local maximum corresponds to the potential vorticity maximum layer associated with an expression of the main thermocline southeast of Japan [*Emery et al.*, 1984; *Qu et al.*, 2001]. The mean profiles at other sites are qualitatively similar to the profile used in "Only M_2-Tide." This issue will be discussed in the next section from a view of possible effects of changing stratification forced by the no-tidal processes on the baroclinic tide variability.

The dissipation dominant feature at Tokara Strait and Izu Ridge is attributable to larger friction due to the relatively shallower depth at which BEC actually occurs. Figure 10 compares the horizontal distributions of BEC averaged for the all subperiods and the bottom topography in the four spots. Large part of BEC around Tokara Strait and Izu Ridge is shown at the depth shallower than 500 m, and the averaged water depths of a region in which BEC rates are larger than 0.2 W m^{-2}, indicated by contours in Figure 10, are 852 and 1107 m at Tokara Strait and Izu Ridge, respectively. In contrast, the large BEC rate in the other two spots is shown in the region with depths ranging from shallow to deep levels, and the averaged depths of a region showing the conversion rates larger than 0.2 W m^{-2} are 1889 and 2046 m at Luzon Strait and Ogasawara Ridge, respectively.

The radiation direction of the baroclinic tidal energy is governed by the characteristic slope defined as $\phi \equiv [(\omega^2-f^2)/(N^2-\omega^2)]^{0.5}$, where ω is the tidal frequency, f is the Coriolis parameter, and N is the buoyancy frequency [*Wunsch*, 1975]. The baroclinic tidal waves incident on the super (sub) critical slope where the difference between the bottom slope and the characteristic slope angles is positive (negative) will propagate toward deeper (shallower) region. The angle difference estimated around the four hot spots (Figure 11) indicates that the large part of the baroclinic tidal energy generated near the subcritical slopes (cf. Figure 10) at the dissipation dominant hot spots (Tokara Strait and Izu Ridge) is radiated into the shallower regions and dissipated there [*Osborne et al.*, 2011]. At the radiation dominant hot spots (Ogasawara Ridge and Luzon Strait), the baroclinic tidal energy is actively generated over the supercritical slopes and thus could be radiated mainly outward into deeper regions from there. Note that the distribution of the angle difference itself shows no significant time dependence (not shown).

4. Modulation of M_2 Internal Tide by the Background Oceanic Conditions

Figure 8 depicts that the temporal variations of both BEC and radiation rates at the hot spots are similar to each other (see correlation between them described in Table 2). The temporal variations are also found in time sequences of supply of depth-integrated (barotropic) tidal energy into four spots (Figure 12 and Table 1), which is defined as

$$-\sum_i \int_{C_i} \langle \overline{P^{bt} U^{bt}}_n D \rangle dl = -\sum_i \int_{C_i} \langle \overline{P^{bt} U^{bt}}_n D \rangle dl|_{positive} - \sum_i \int_{C_i} \langle \overline{P^{bt} U^{bt}}_n D \rangle dl|_{negative}, \quad (4)$$

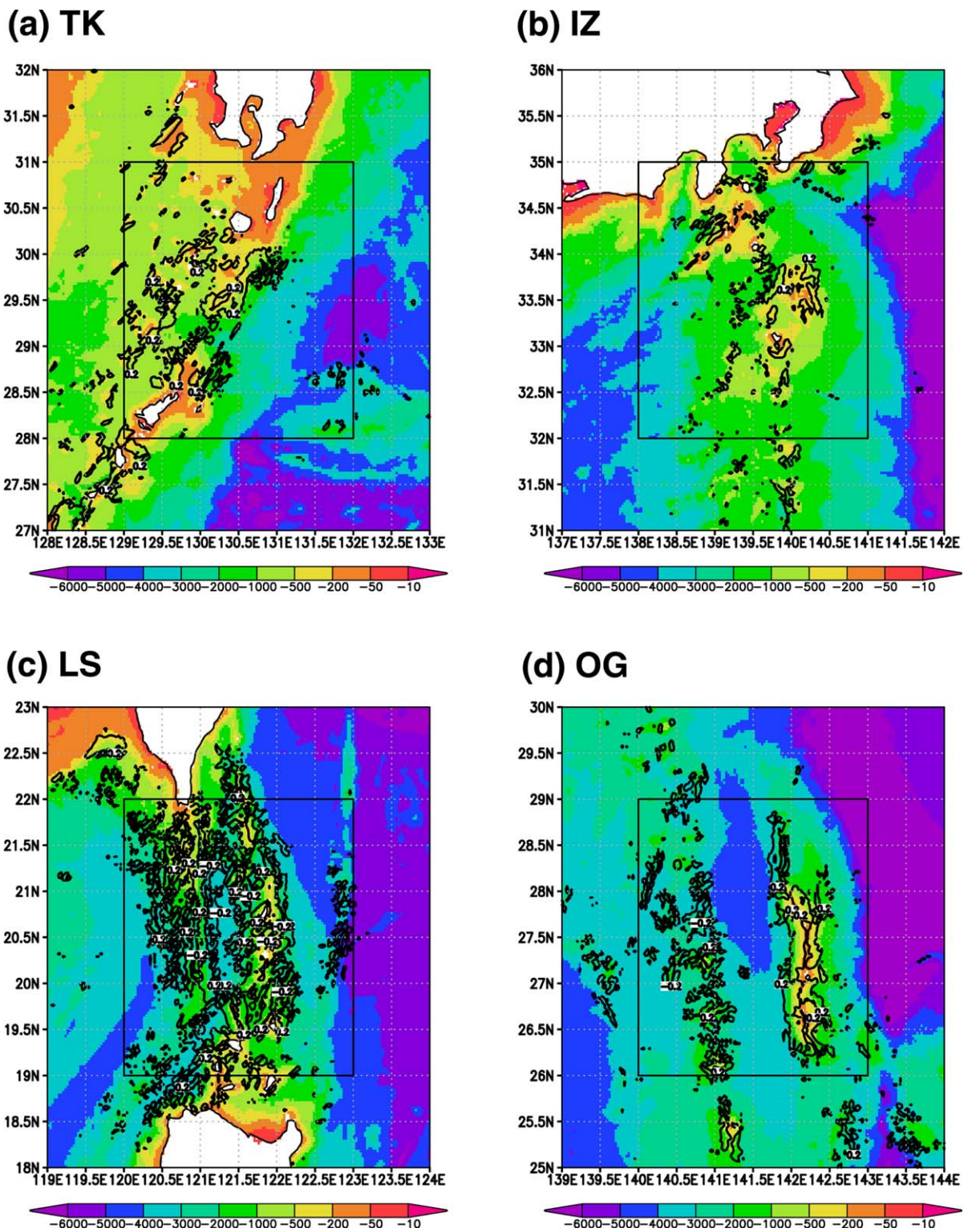

Figure 10. Zoom up views of the time-mean depth-integrated BEC rate of 0.2 W m^{-2} denoted by contours around the hot spots. Shade denotes the bottom topography (in m). The square denotes each hot spot area. Isodepth lines with 500 and 1000 m are indicated by solid contours. (a) Tokara Strait, (b) Izu Ridge, (c) Luzon Strait, and (d) Ogasawara Ridge.

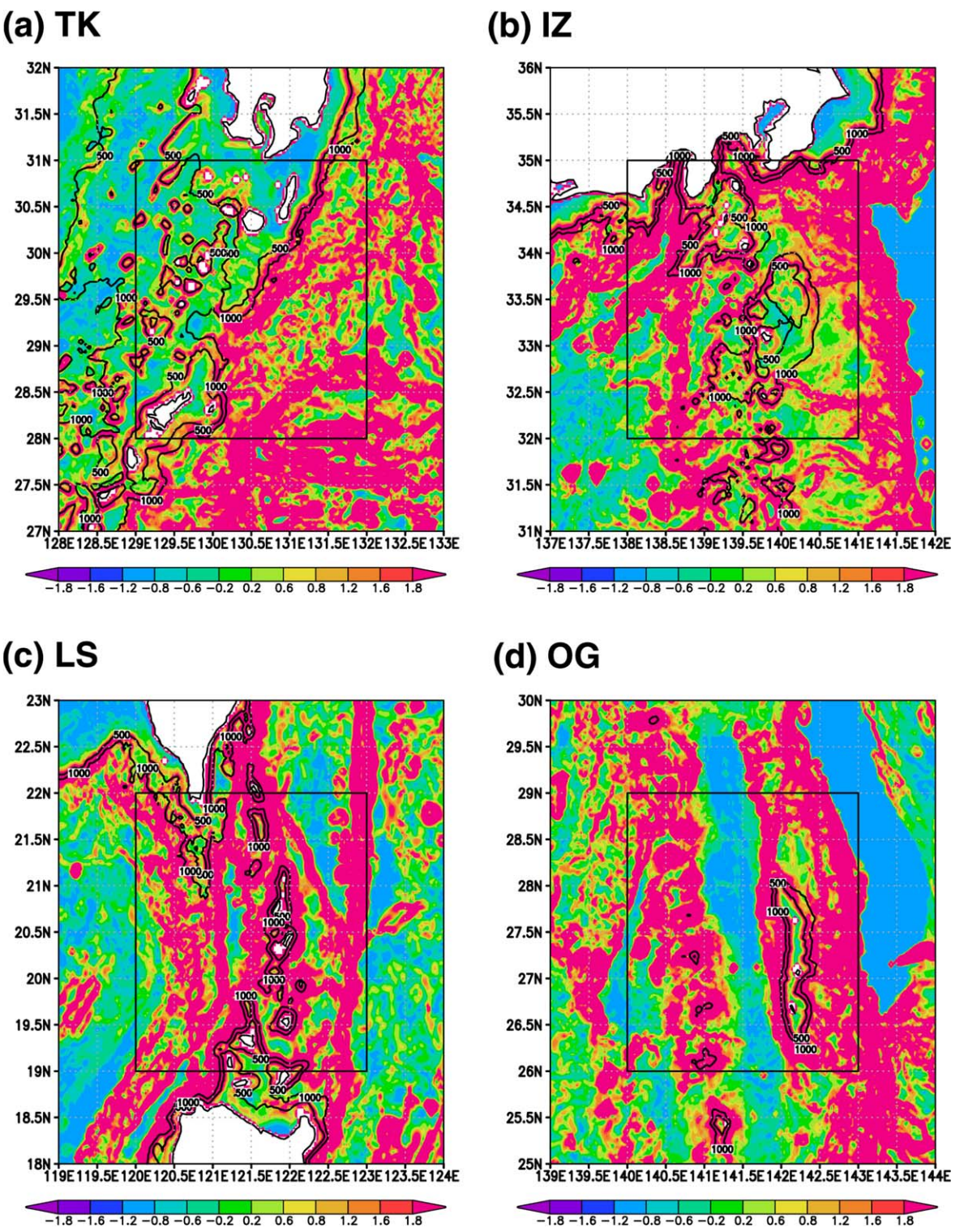

Figure 11. As in Figure 10 except for the contours denoting the isobath lines of 500 and 1000 m and the shade denoting the angle difference (in degree) between the bottom and characteristic slopes.

where $-\sum_i \int_{C_i} F dl|_{positive(negative)}$ means a summation of integrated flux values with positive (negative) signs (F) among four lateral boundaries, $C_i (i=1, 2, 3, 4)$, defining a hot spot region and positive (negative) means supply of the energy into (radiation of the energy from) the spot through the boundary. P^{bt} and U_n^{bt} denote barotropic pressure and barotropic (depth-averaged) velocity outward normal to the boundary. BEC seems

Table 2. Correlation Coefficients for M_2 BEC Rate Averaged in the Spots With the Divergence of the Depth-Integrated Tidal Energy Flux at the Spots (Radiation), the Depth-Integrated Tidal Energy Supply Into the Spots (Supply), the EOF Amplitudes of the Buoyancy Frequency Profiles Horizontally Averaged in the Spots (EOF), and Buoyancy Frequency at Selected Depths Averaged in the Spots (BVF)[a]

	Tokara Strait	Izu Ridge	Luzon Strait	Ogasawara Ridge
Radiation	**0.61**	**0.68**	**0.68**	**0.51**
Supply	**−0.42**	**0.29**	**0.56**	0.24
EOF1	0.19 (72)	**0.50** (77)	**−0.44** (72)	0.04 (65)
EOF2	**0.62** (20)	**0.38** (18)	**−0.40** (22)	0.15 (28)
EOF3	**0.62** (5)	0.03 (3)	0.02 (4)	0.04 (4)
EOF4	0.19 (2)	0.12 (1)	0.08 (1)	0.10 (2)
EOF5	0.07 (0.8)	0.05 (0.5)	0.27 (0.4)	**0.50** (0.5)
EOF6	0.00 (0.1)	0.14 (0.2)	0.04 (0.1)	**0.40** (0.07)
BVF50m	0.00	**0.50**	**−0.56**	−0.04
BVF100m	**0.51**	**0.62**	**−0.50**	−0.03
BVF200m	**0.79**	**0.48**	**−0.59**	**−0.52**
BVF500m	**−0.52**	0.05	−0.04	**0.52**
BVF800m	**−0.55**	0.15	**0.34**	**0.48**
BVF1000m	−0.24	0.13	**0.29**	**0.38**

[a]The significant correlation level is 0.27 for $p < 0.01$ and the significant correlation values are indicated by the bold font. Numerics in parentheses of the EOF modes cells denote the contribution ratios (in %) of the EOF modes to the total variance.

to temporally vary partly responding to the variation of the supply of the depth-integrated tidal energy at Luzon Strait (thick curves shown in Figure 12c). The depth-integrated energy supply into the spot converges to the steady state in after the initial adjustment in "Only M_2-Tide" (not shown) since the background stratification also converges to the steady state. The significant spatiotemporal variation of the stratification induced by the ocean circulation affects the baroclinic tide generation and radiation at all generation sites, and thus the depth-integrated tidal energy flux experiences the spatiotemporal variation as a result of the variation in BEC occurring over all generation sites included in the model region. This effect is considered as

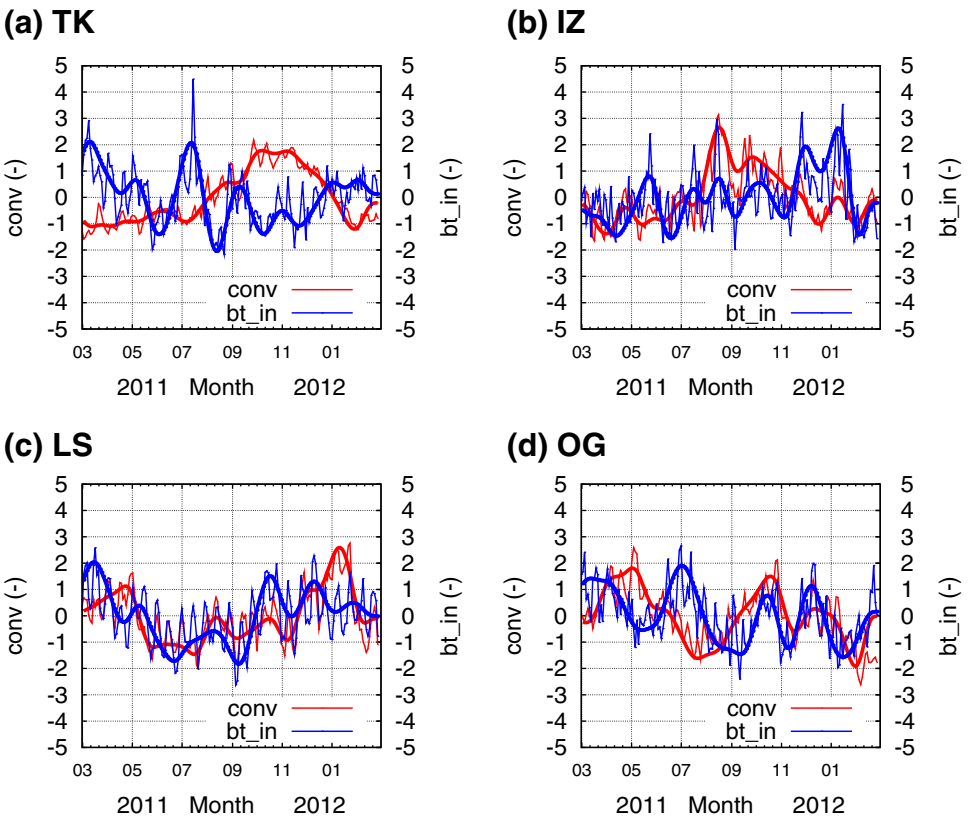

Figure 12. Time sequences of BEC rate (red curves) averaged in the spots and the barotropic tidal energy supply into the spots (blue curves). (a) Tokara Strait, (b) Izu Ridge, (c) Luzon Strait, and (d) Ogasawara Ridge. Thin curves denote the 3 day subperiod sequences normalized by mean and standard deviation for the all subperiods and thick curves denote their low-pass filtered sequences with a cutoff at 30 day period.

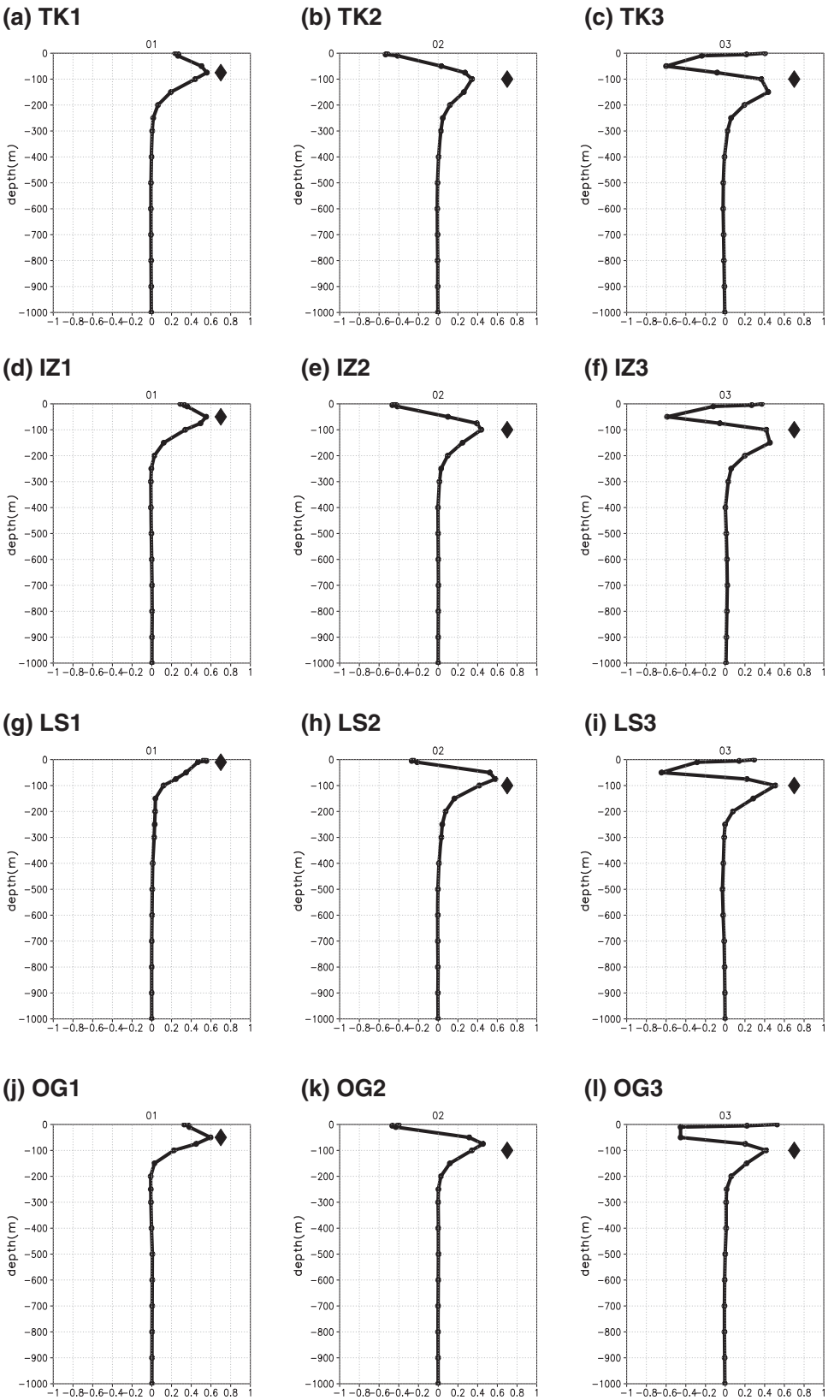

Figure 13. EOF mode profiles obtained from the buoyancy frequency averaged at the hot spots. (a) Mode 1, (b) Mode 2, and (c) Mode 3 for Tokara Strait; (d) Mode 1, (e) Mode 2, and (f) Mode 3 for Izu Ridge; (g) Mode 1, (h) Mode 2, and (i) Mode 3 for Luzon Strait; and (i) Mode 1, (j) Mode 2, (k) Mode 3 for Ogasawara Ridge.

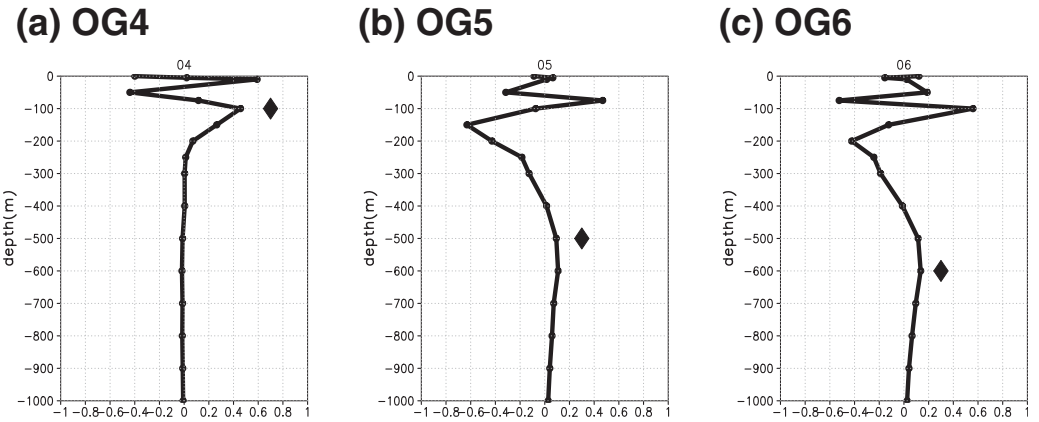

Figure 14. As in Figure 13 except for (a) Mode 4, (b) Mode 5, and (c) Mode 6 for Ogasawara Ridge.

the remote effect of the varying background stratification on the baroclinic tide generation at a local generation site. Luzon Strait shows the highest correlation value (0.56) between the supply of the depth-integrated tidal energy and BEC among the four spots (Table 2), suggesting the significance of the remote effect there as demonstrated also by *Kerry et al*. [2011, 2014]. The other spots, however, indicate low levels of positive correlation values (Izu Ridge and Ogasawara Ridge) and a negative value (Tokara Strait). Later we examine this issue by using the multi regression analysis allowing consideration of mutual relationship among all explanatory variables.

Since the intensity of BEC is also affected by the local background stratification [*Petrelis et al*., 2006] at a local region, we examine relations between the buoyancy frequency, $N=\sqrt{\frac{g}{\rho_0}\frac{\partial\rho}{\partial z}}$ (z is positive value of depth, g is gravity acceleration, and ρ_0 is reference density), and BEC rate. Temporal variations of the buoyancy frequency profile spatially averaged in each spot are decomposed into Empirical Orthogonal Function (EOF) modes [*Kutzbach*, 1967]. The first three EOF modes at the four spots indicate similar profiles among each other (Figure 13). The first mode represents the variability of the stratification in the upper 200 m depth, and the second and third modes represent the variability in the upper 300 m depths. Although some EOF modes have multiple local maxima with positive and negative signs, we focus on the positive correlation for the positive local maximum at the deepest level (see closed diamonds denoted in Figures 13–15), because BEC occurs around the bottom slope. Results summarized in Table 2 indicate statistically significant correlation values between BEC and some EOF modes for each spot: second and third modes at Tokara Strait (Figures 13b and 13c), first and second modes at Izu Ridge (Figures 13d and 13e), first and second modes at Luzon Strait (Figures 13g and 13h), and fifth and sixth modes at Ogasawara Ridge (Figures 14a and 14b). The positive correlation of the lower modes for Tokara Strait and Izu Ridge implies that the

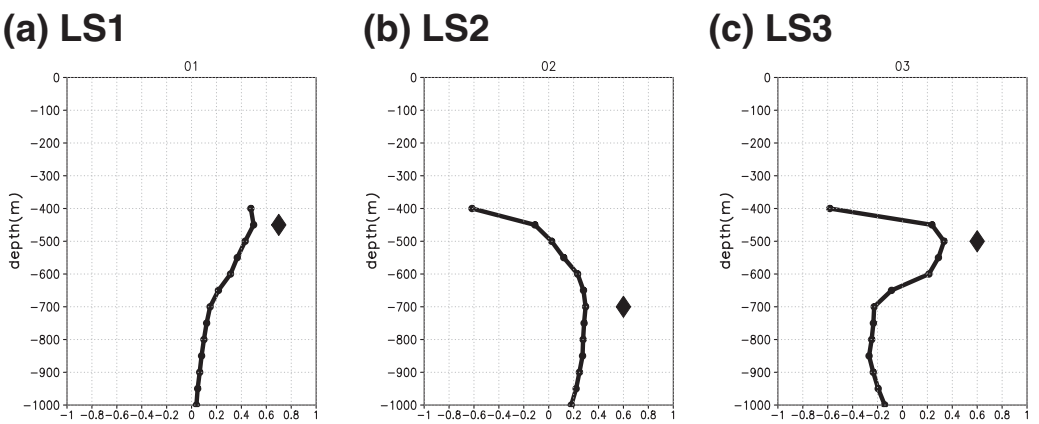

Figure 15. EOF mode profiles obtained from the buoyancy frequency below 400 m averaged at Luzon Strait. (a) Mode 1, (b) Mode 2, and (c) Mode 3.

Table 3. As in Table 2 Except for the Correlation for BEC Rate With the EOF Modes of the Buoyancy Frequency Profiles Below 400 m Horizontally Averaged at Luzon Strait

	Luzon Strait
EOF1b	−0.15 (79)
EOF2b	**0.58** (17)
EOF3b	0.08 (2)
EOF4b	**0.31** (0.5)
EOF5b	0.09 (0.2)
EOF6b	0.17 (0.07)

increase of the stratification intensity in the layer at some depths between surface and 300 m corresponds to the increase of BEC rate (see positive maxima shown in Figures 13b–13e), and this relation is confirmed by the significant positive correlation of the buoyancy frequency at the near surface levels (Table 2). Such correlation representing the effect of the near surface stratification is consistent with the fact that BEC occurs around relatively shallow slope at Tokara Strait and Izu Ridge (Figures 10a and 10b).

At Luzon Strait, significant negative correlation values are found for the first and second mode amplitudes and the buoyancy frequency values in the near surface layer, while the fifth mode amplitude and the buoyancy frequency in the deeper layer show positive correlation. To detect the effects of the stratification in the deeper layer more clearly, we conduct the EOF analysis of the profile below 400 m (Figure 15). Later we discuss

Table 4. Normalized Partial Regression Coefficients for BEC Rate at the Spots With the Depth-Integrated Tidal Energy Supply Into the Spots and the EOF Modes of the Buoyancy Frequency Averaged at the Spots[a]

	Tokara Strait	Izu Ridge	Luzon Strait Below 400 m	Ogasawara Ridge
Supply (t)	−0.05 (−1.7)	0.28 (5.1)	0.36 (4.2)	0.09 (1.3)
EOF1 (t)	0.21 (9.4)	0.46 (9.8)	0.11 (1.8)	0.05 (0.59)
EOF2 (t)	0.50 (22)	0.90 (13)	0.61 (11)	0.35 (3.2)
EOF3 (t)	0.58 (16)	0.59 (8.0)	0.24 (4.2)	0.23 (1.8)
EOF4 (t)	0.20 (11)	0.36 (6.6)	0.20 (2.9)	0.003 (0.034)
EOF5 (t)	0.03 (1.5)	0.15 (2.6)	0.09 (1.7)	0.54 (7.6)
EOF6 (t)	0.11 (4.6)	0.11 (2.4)	0.03 (0.52)	0.30 (3.8)
AR2 (F)	0.98 (670)	0.87 (85)	0.73 (36)	0.65 (24)

[a]Numerics in parentheses of the cells denote the *t*-values of the regression coefficients. Cells in the lowest row denote the adjusted R squared (AR2) and F (in parentheses) values of the multiregression.

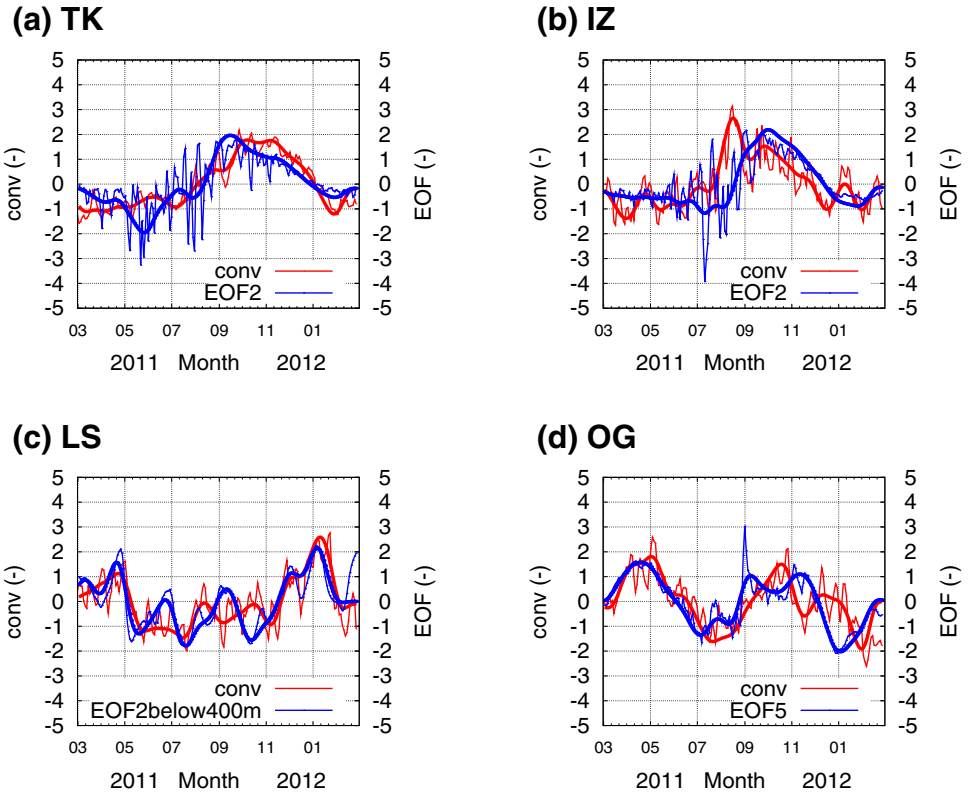

Figure 16. As in Figure 12 except for blue curves denoting the amplitude of the selected EOF modes at the spots (see the text for the definition).

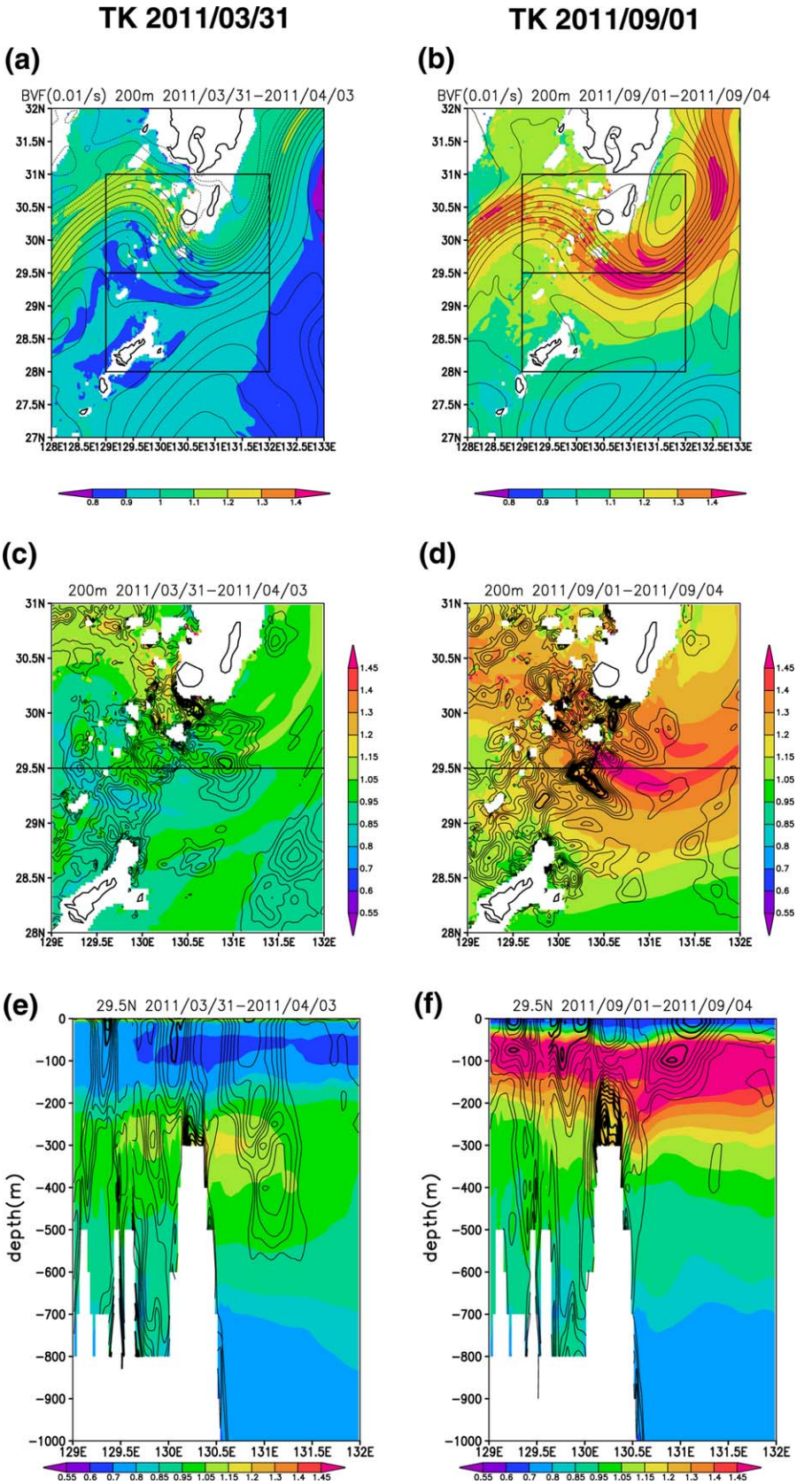
TK 2011/03/31
TK 2011/09/01
(a)
BVF(0.01/s) 200m 2011/03/31–2011/04/03
(b)
BVF(0.01/s) 200m 2011/09/01–2011/09/04
(c)
200m 2011/03/31–2011/04/03
(d)
200m 2011/09/01–2011/09/04
(e)
29.5N 2011/03/31–2011/04/03
(f)
29.5N 2011/09/01–2011/09/04
depth(m)

Figure 17.

possible implications suggested by significant positive correlation found in the second mode (Table 3). At Ogasawara Ridge, the fifth and sixth modes with local positive maxima at 500–600 m depths (see closed diamonds shown in Figures 14b and 14c) show significant positive correlation, but the lower modes indicate no significant correlation. Later we also discuss roles of the stratification around 500 m depth in the BEC modulation at Ogasawara Ridge, which is also suggested from the comparison of the "Only M_2-Tide" and "M_2-Tide" results (see Figures 8d and 9).

The correlation analysis described above implies that the varying background stratification affects BEC remotely through the supply of the depth-integrated tidal energy into the spot and locally through the local stratification represented by the EOF modes at the spot. To clarify roles of both the remote and local effects in the temporal variation of the energy conversion, we conduct the multi regression analysis using all relevant variables (Table 4). High-frequency variations with period shorter than 30 days are removed by low-pass filtering from all variables to focus on the mesoscale and/or seasonal variability. The analysis results for the four spots generally lead to high values of the determination coefficient (adjusted R squared) and F-statistic. At Tokara Strait, the negative correlation between the supply of the depth-integrated tidal energy and BEC is statistically insignificant. Both second and third modes show the relatively large partial regression coefficients and *t*-values compared to the other EOF modes. For Izu Ridge the significance of the first, second, and third modes is evident. At Luzon Strait, the second EOF mode for the stratification below 400 m is most significant, and the supply of the depth-integrated tidal energy secondarily contributes to the variability of BEC. At Ogasawara Ridge, the fifth and sixth modes are comparatively significant among the all EOF modes.

Based on the statistical analyses described above, we conclude that the most significant local stratification factors at the four spots are represented by the EOF second mode (Tokara Strait and Izu Ridge), the fifth mode (Ogasawara Ridge), and the second mode for stratification below 400 m depth (Luzon Strait). A typical positive impact of the local stratification factor on BEC is recognized by identifying an oceanic condition at each hot spot when the BEC rate increases anomalously with intensified local stratification. Using the time sequences of EOF amplitudes for the stratification and the BEC rate (Figure 16), both normalized by temporal means and standard deviations (Table 1), we define the locally enhanced (weakened) states as in cases of (1) the normalized conversion rate $>+1.2$ (<-1.2) and (2) the normalized EOF amplitude $>+1.2$ (<-1.2).

Figures 17a and 17b compare the locally weakened and intensified states of the stratification at 200 m depth around Tokara Strait. Correspondence between the stratification and the activated M_2 tidal currents, which is represented by the band-pass filtered current magnitude with the target period from 11 to 14 h (note that the minimum period of the inertial motion over the model region is approximately 15.6 h), is exhibited in Figures 17c–17f. The enhanced stratification is distributed around the Kuroshio small meander (Figure 17b) formed during the period from September to December 2011. The strong stratification is confined in the layer at depths between 50 and 200 m, and the tidal current is activated in the strong stratification layer (Figure 17f). In contrast, the activation of the tidal current is attenuated in the weak stratification layer, particularly in the mixed layer enhanced by the winter mixing (Figure 17e). The horizontal distribution of the tidal currents seems to be affected by the Kuroshio path (Figures 17c and 17d).

Similarly, the Kuroshio path variation affects the stratification around Izu Ridge (Figure 18). The tidal currents are enhanced along the Kuroshio small meander path formed during the period from September to October 2011 (Figure 18d), and the enhancement is confined in the strong stratification layer (Figures 18f). The stratification in the subsurface layer at both Tokara Strait and Izu Ridge is enhanced by the cyclonic eddy associated with the Kuroshio small meander. Such enhancement of the stratification due to the cyclonic eddies is also observed over the North Western Pacific [*Kouketsu et al.*, 2012]. The periods of the positive maxima shown in the lower-frequency variations of the EOF second mode amplitude at each spot (see blue thick curves in Figures 16a and 16b) generally correspond to the periods of the Kuroshio small meander occurrence there (not shown). Note that the not only the Kuroshio path variation but also the seasonal

Figure 17. Time-mean buoyancy frequency (shade; in s^{-1}) at 200 m depth for the subperiods showing the (a) typical locally weakened and (b) enhanced BEC states among the all subperiods. Contours denote the time-mean sea surface height with interval of 0.05 m for the subperiods. A box indicates the region of the Tokara Strait spot. (c, d) Zoom up views of the Tokara Strait spot showing the time-mean buoyancy frequency (shade; in s^{-1}) at 200 m depth for the subperiods showing the typical locally (Figure 17c) weakened and (Figure 17d) enhanced BEC states among the all subperiods. Contours denote the root mean square variability (0.02–0.10 m s^{-1}) of the band-pass filtered current with the target period from 11 to 14 h. Contour interval is 0.005 m s^{-1} and thick contours denote the values upper 0.05 m s^{-1}. (e) As in Figure 17c except for showing a vertical section along 29.5°N, which is denoted by horizontal lines in Figures 17a–17d. (f) As in Figure 17d except for showing a vertical section along 29.5°N.

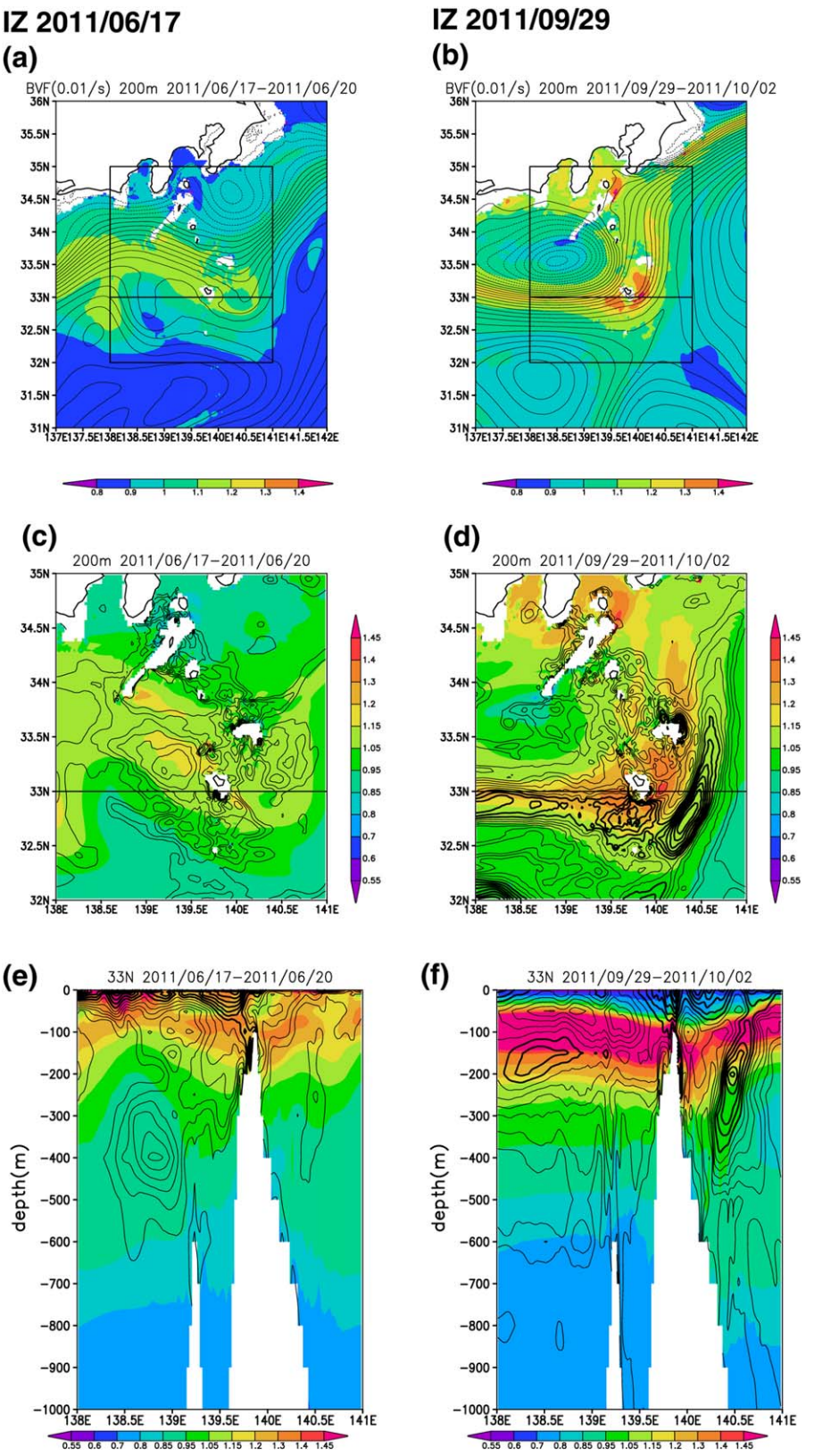

Figure 18. As in Figure 17 except for showing the similar conditions of the (a, c, e) enhanced and (b, d, f) weakened BEC states around Izu Ridge.

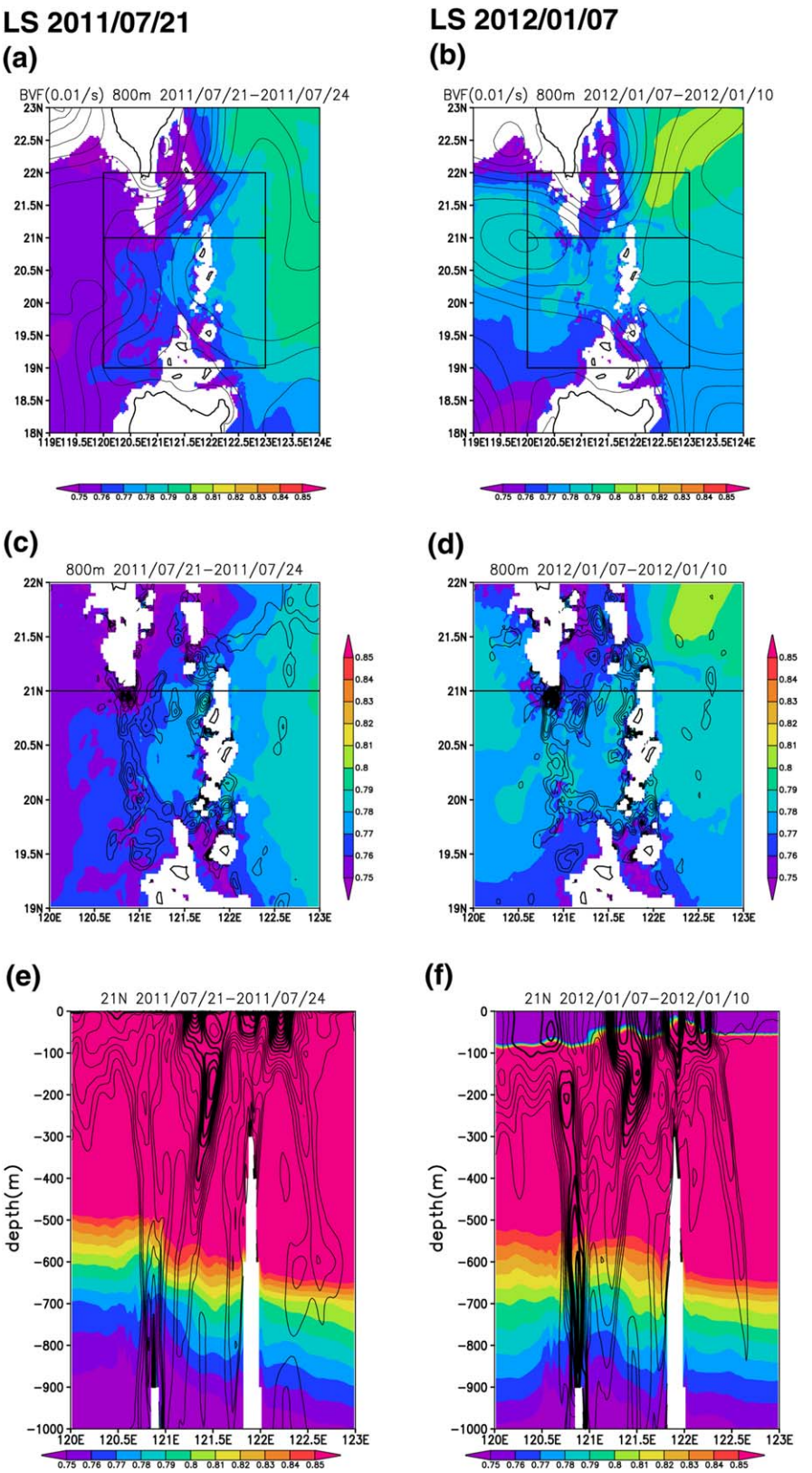

Figure 19. As in Figure 17 except for showing the similar conditions of the (a, c, e) enhanced and (b, d, f) weakened BEC states around Luzon Strait. Figures 19a–d show the states at 800 m depth.

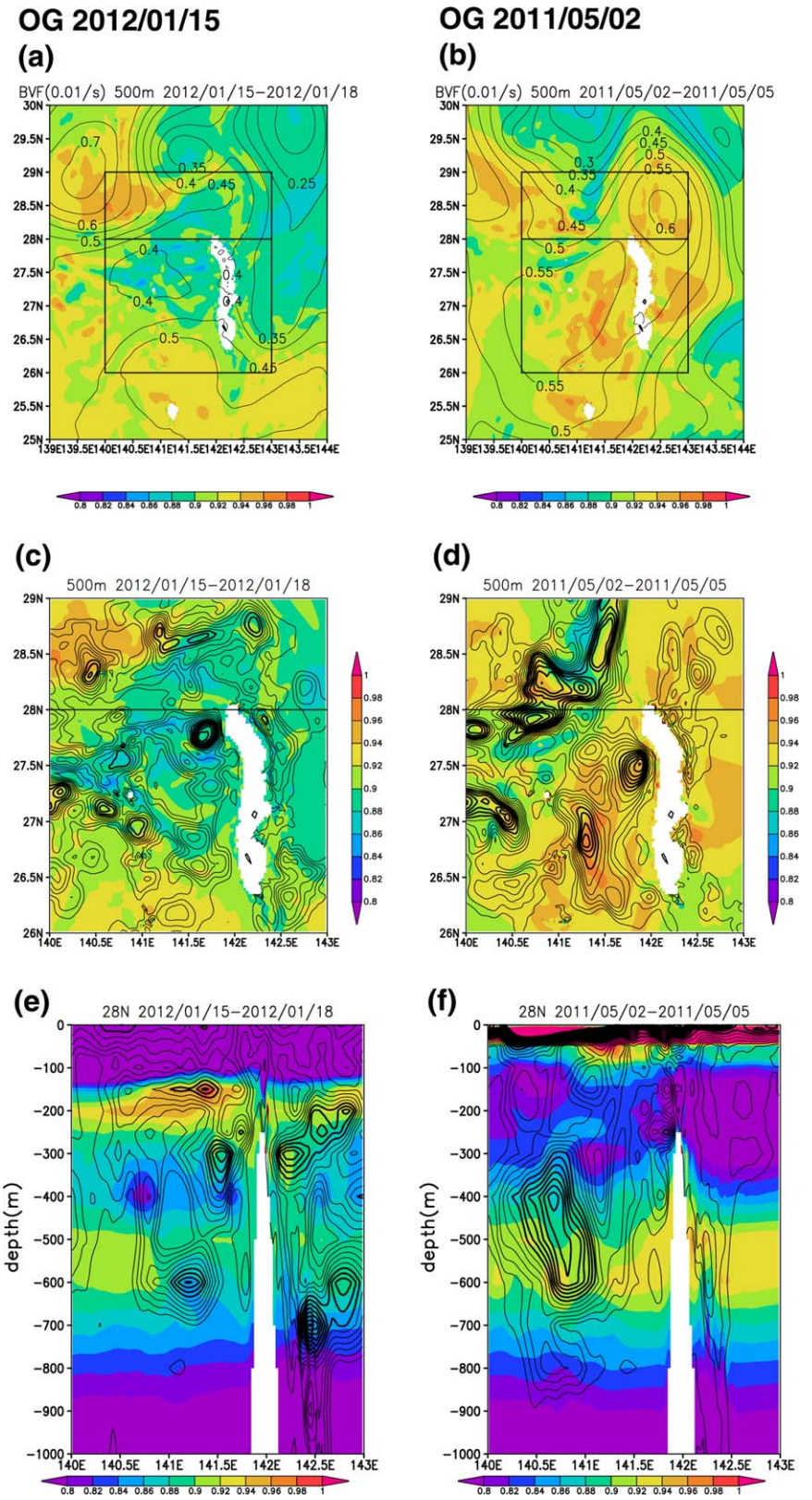

Figure 20. As in Figure 17 except for showing the similar conditions of the (a, c, e) enhanced and (b, d, f) weakened BEC states around Ogasawara Ridge. Figures 20a–20d show the states at 500 m depth.

thermocline variation also affects the BEC variation; in fact, the enhanced BEC gradually declines as shown in Figures 16a and 16b after the beginning of the cooling season even during the period when the Kuroshio small meander state continues.

Around Luzon Strait, the Kuroshio path alternatively takes the looping and leaping modes [*Sheu et al*., 2010]. The former modes represents the westward Kuroshio intrusion into South China Sea through Luzon Strait, while the Kuroshio tends to flow northward without intrusion during the latter mode period. The enhanced BEC actually occurs during the two intrusion periods (April 2011 and January 2012), which are indicated by the positive maxima of the EOF second mode amplitude for the stratification below 400 m depth (Figure 16c). Figure 19b represents the locally enhanced state in January 2012, during which the enhanced tidal currents appear around the western part of the ridges, especially at 21°N, 121°E (Figure 19d). The stratification at 800 m depth is strengthened together with the Kuroshio intrusion (Figure 19f). It is known that the Kuroshio intrusion accompanies the high potential vorticity water (roughly corresponding to the strong stratification) around the bottom of the main thermocline [*Qu et al*., 2001]. Similar enhancement of the baroclinic tide generation at Luzon Strait is demonstrated using another ocean model [*Kerry et al*., 2014, Figure 10].

During the leaping mode period of July 2011 (Figure 19a), the tidal current around the western ridge is comparatively suppressed (Figures 19c and 19e). *Sheu et al*. [2010] suggest that the leaping (looping) mode tends to appear in summertime (wintertime). The weakened (enhanced) BEC state actually occurs in summertime (wintertime) in the present simulation showing the similar seasonal occurrence of the Kuroshio intrusion. The negative correlation of the lower EOF modes showing the seasonal variation of the stratification in the near surface layer (enhanced in summertime and weakened in wintertime) might appear owing to the dominant effect of the deep stratification controlled by the seasonally phase-locked Kuroshio intrusion.

Although there exist no Kuroshio variability around Ogasawara Ridge, the mesoscale eddy activity affects the baroclinic tide activity through the varying background stratification near the main thermocline there (Figure 20). Comparison of a time sequence of sea surface height anomaly averaged in Ogasawara Ridge (not shown) and that of the fifth EOF mode amplitude (Figure 16d) indicates that the positive high values of the EOF mode corresponds to the events of the anticyclonic eddies passing around there. The locally intensified BEC state appears in the beginning of May 2011, and the local stratification maximum around the bottom of the main thermocline [*Qu et al*., 2001] induced by deepening of the thermocline depth associated with the passing of an anticyclonic eddy covers the whole spot region (Figure 20b). The tidal current enhancement is shown in the layer with the local maximum of the stratification intensity (Figure 20f). The role of the stratification around the bottom of the main thermocline depth in the energy conversion is also suggested from the result of the sensitivity experiment (Figure 8d) with the horizontally uniform stratification profile (Figure 9) that has not the local maxima of the buoyancy frequency near the 500 m depth around Ogasawara Ridge.

Distributions of the radiation flux of M_2 baroclinic energy exhibit the variations of the energy flux in the corresponding subperiods with the locally weakened and intensified states (not shown). The all spots show considerable differences in the radiation flux distributions between the locally weakened and intensified states. The radiation flux distribution represents quite complicated patterns. The energy radiation of the baroclinic tide is locally enhanced even in the generally weakened state, indicating that the energy radiation of the baroclinic tide is not simply governed by BEC variation but also is affected by the local dissipation and advection inside of the spot [*Pereira et al*., 2007; *Chavanne et al*., 2010; *Jan et al*., 2012].

5. Summary and Discussion

We conducted a 1 year concurrent simulation of the ocean circulation and tide in the Western North Pacific using an ocean general circulation model with a horizontal resolution of 1/36° to investigate possible interactions between the circulation and tide. The model reproduces the amplitude and phase of M_2 tide as observed in the open ocean portion. It also reproduces some part of the amplitude of M_2 tidal harmonics evaluated from the high-pass filtered sea surface height anomaly, which could be regarded as the surface manifestation of the baroclinic tide. In particular, the intense variability of the M_2 baroclinic tide harmonics around Tokara Strait, Izu Ridge, Luzon Strait, and Ogasawara Ridge (the hot spots) are represented by the model nearly as observed.

The sensitivity experiment simulations forced by the only M_2 tidal constituent allows the calculation of M_2 harmonics for a short-term (3 day) period. Intensity of the M_2 barotropic to baroclinic energy conversion (BEC) rates at the hot spots evaluated from the harmonics in each 3 day subperiod exhibits the time dependence attributable to the temporal variations of the background stratification. The result suggests that the temporal variation of the local stratification intensity could be a proxy of the bulk estimate of the temporal variation of BEC in the spot, though the remote fluctuation of the depth-integrated tidal energy supply into the spot partly affects it.

The EOF analysis of the buoyancy frequency averaged at the spot indicates the temporal variations of some EOF modes correlate with the variation of BEC averaged there. Characteristics of the most dominantly influential mode at each spot imply the lower-frequency oceanic phenomena that are mainly responsible for modulating the baroclinic tide variability there through changes in intensity of the local stratification. At Tokara Strait and Izu Ridge, the enhanced stratification in the upper thermocline layer caused by the development of the Kuroshio small meander together with the seasonal thermocline variation considerably affects the temporal variation of BEC. At Luzon Strait and Ogasawara Ridge, the energy conversion is modulated by the variations in the stratification around the bottom of the main thermocline governed by the Kuroshio intrusion into the South China Sea (Luzon Strait) and the mesoscale eddy activity (Ogasawara Ridge). Note that the remote effect due to the temporal variation of the depth-integrated tidal energy supply, which is caused by BEC occurring over the all baroclinic tide generation sites, is not negligible especially at Luzon Strait, as suggested also by the previous studies [*Kerry et al*., 2013, 2014].

BEC mainly occurs over the bottom slope at the relatively shallow depth at Tokara Strait and Izu Ridge, and thus most of the baroclinic tidal energy is locally dissipated and the stratification in the relatively shallow layer is crucial for the modulation of the baroclinic tide generation. At the other two spots, in contrast, the radiation of the baroclinic tidal energy is more active than at the former spots because of the relatively deep bottom slope where the active energy conversion occurs, and the stratification in the relatively deep layer is influential in the modulation of the baroclinic tide generation.

The multiregression using the stratification intensity and depth-integrated tidal energy supply does not completely explain the variance of the found energy conversion; in particular, the explained ratio is relatively low at the radiation dominant hot spots: Luzon Strait and Ogasawara Ridge (Table 4). The roles of the fluctuation of the depth-integrated energy supply in the energy conversion might be different among the spots as suggested by the values of the normalized partial regression coefficients. Detailed BEC processes could be affected by the additional contribution from the local dissipation and advection [*Jan et al*., 2012]. Divergence of M_2 baroclinic energy radiation flux varies in time responding to the variation of the conversion rate, and its variation range is larger than that of the conversion rate at the radiation dominant sites (Figure 8) also due to the effects of the local dissipation and advection [*Pereira et al*., 2007; *Chavanne et al*., 2010; *Jan et al*., 2012]. Evaluation of possible effects of such local processes on the tidal energetics in the hot spots might be influenced by the horizontal and vertical resolution used in the model and still has not been examined so far, though only the rough estimate of the dependence based on the empirical relationship between BEC rate and the horizontal resolution has been done [*Niwa and Hibiya*, 2011]. Future studies await further exploration in these directions.

Appendix A: Details of the Tidal Forcing in the Simulation

Tidal processes are introduced into the regional JCOPE-T model by counting both the tidal gravity force in the model momentum equations and the open boundary condition including the tidal volume fluxes and tidal sea level elevations provided from existing barotropic tidal models. The equilibrium surface pressure gradient induced by 21 tidal potential constituents: Q_1, O_1, M_1, P_1, K_1, J_1, OO_1, $2N_2$, MU_2, N_2, NU_2, M_2, I_2, T_2, S_2, K_2, MM, MF, SSA, SA, MTM, and MSQM is added to the surface pressure gradient term for the operational ocean forecasting. Tidal forcing composed of eight constituents: Q_1, O_1, P_1, K_1, N_2, M_2, S_2, and K_2, is included in JCOPE-T as volume fluxes and sea level anomaly provided from Oregon State University Tidal Inversion Software (OTIS) [*Egbert and Erofeeva*, 2002] at lateral boundaries.

Tidal gravity force is estimated using the tidal potential provided as an equilibrium tide sea surface elevation amplitudes for major tidal harmonics. Total equilibrium tide height is estimated integrating potentials of selected tide harmonics and using corresponding analytical formulas for the space distribution and time

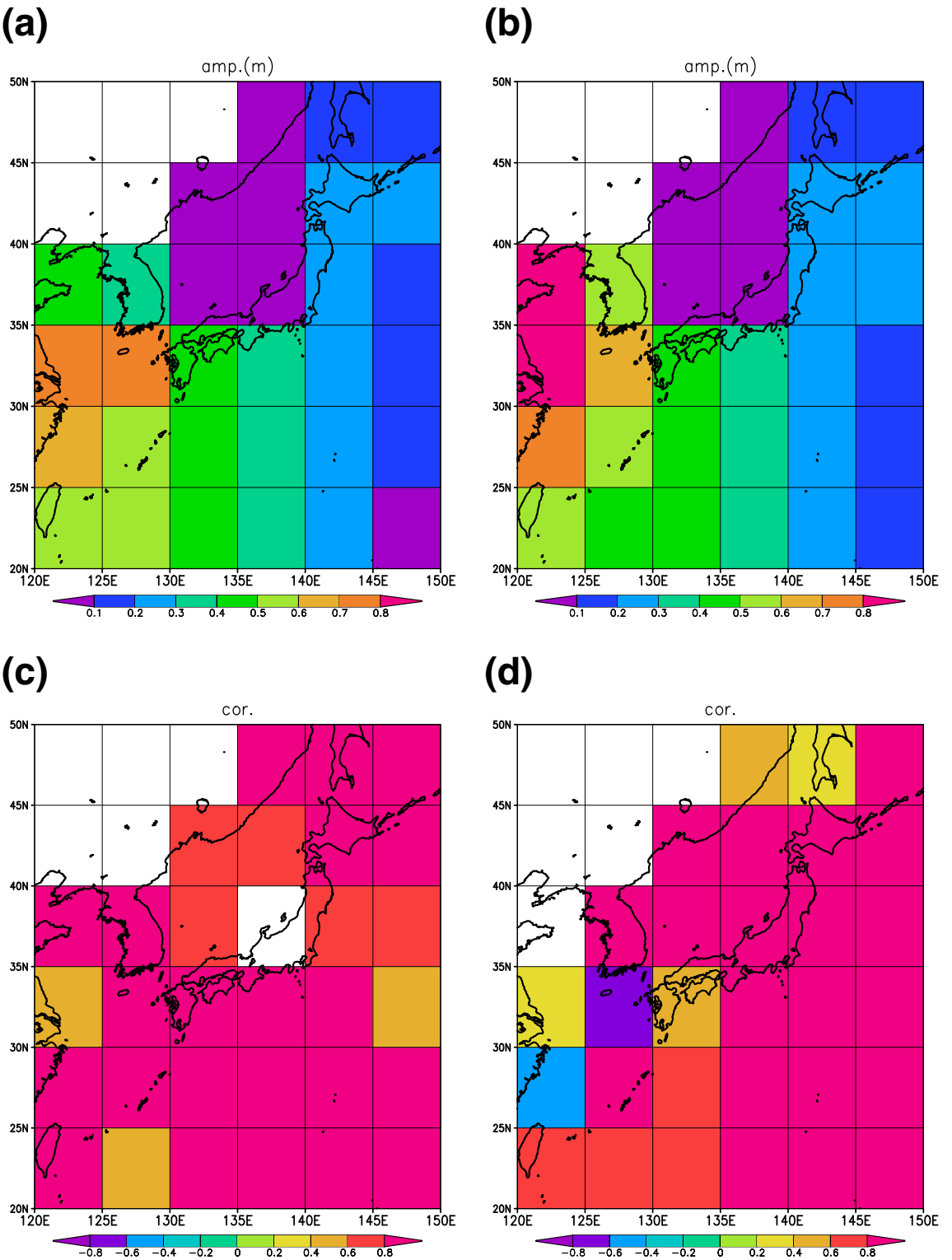

Figure A1. (a) M_2 tidal amplitudes (in m) evaluated from sea surface height anomaly along the Jason-2 tracks averaged in square regions of 5° by 5°. (b) The Jason-2 observation data. (right) The JCOPE-T simulation data. (c) Correlation between the M_2 tidal amplitude of the Jason-2 observation and JCOPE-T simulation evaluated along the Jason-2 tracks within square regions of 5° by 5°. Statistically insignificant regions are excluded from the shading. (d) As in Figure A1c except for phase.

variability (frequency and phases) of considered harmonics [e.g., *Kantha and Clayson*, 2000]. Then the pressure gradient term in the model momentum conservation equations related with the sea level distribution is replaced by the term that counts for the presence of tidal gravity force provided as distribution of the total equilibrium sea surface height,

$$\frac{\partial \eta}{\partial x_i} \rightarrow \frac{\partial(\eta - \eta et)}{\partial x_i}, \tag{A1}$$

where x_i correspond to two model horizontal axes ($i = 1,2$), η is the model sea surface height, η_{et} is an equilibrium tide height defined as function of time and location using analytical astronomical relations. We use an equilibrium tide height values for the considered tidal harmonics taken from *Kantha and Clayson* [2000]. Although the tidal gravity force is the main reason for the tide generation in the world ocean, the impact of tidal gravity force in (A1) usually is not significant for the regional models including JCOPE-T owing to the relatively long tidal wavelength of over 1000 km.

We have complex superposition of the tidal gravity waves entering and leaving model domain through open boundaries, and hence need to utilize both tidal volume fluxes and elevations information for getting the best practical solution. Some existing tidal models like OTIS [*Egbert and Erofeeva*, 2002] provide information on tidal volume fluxes and sea level elevations for the world ocean.

The tidal sea level anomalies along open boundaries estimated one step forward in time t + 1 (η_{tide}^{t+1}) are included as a Newtonian smoother relaxation form with a relaxation parameter α_E,

$$\eta^{t+1} = \eta_*^{t+1} + \alpha_E[(\eta_{tide}^{t+1} + \eta_{no-tide}^{t+1}) - \eta_*^{t+1}], \tag{A2}$$

where η_*^{t+1} and η^{t+1} are the first guess and corrected estimates for the forward time step t + 1, respectively, and $\eta_{no-tide}^{t+1}$ is the external nontidal model sea level at the boundary point for the same time step. The tidal sea level boundary conditions (A2) must be specified in the model internal points closest to the open boundary because sea levels defined at the external model boundary have no impact on the model variables. At each time step the sea level in the model cell adjacent to the open boundary is changed from its first guess volume's conservative predicted value (η_*^{t+1}) found by integration of the continuity equation to a value (η^{t+1}) closer to the prescribed sea levels by adding the adjustment term of equation (A2), $\Delta\eta_{adj} = \alpha_E[(\eta_{tide}^{t+1} + \eta_{no-tide}^{t+1}) - \eta_*^{t+1}]$.

For restoring the volume conservation, the boundary volume inflow at time step t that was used for sea level forward-estimation should be corrected to balance the boundary cell volume change $\Delta\eta_{adj} \cdot dS$ where dS is a model cell surface area. Required normal to open boundary barotropic velocity correction is

$$\Delta U_{adj} = \pm \frac{\Delta\eta_{adj} \cdot dS}{(H + \eta^{t+1}) \cdot dl_b \cdot \Delta t}, \tag{A3}$$

where H and dl_b are the undisturbed depth and linear cell size along the open boundary, respectively, and Δt is the integration time step. The sign in (A3) depends on the position of the open boundary; for standard Cartesian coordinate system we will have plus at the western and southern boundaries of domain and minus at the eastern and northern boundaries. The corrected value U_b for the normal to the boundary inflow velocity becomes

$$U_b = U_{no-tide} + U_{tide} + \Delta U_{adj}, \tag{A4}$$

where $U_{no-tide}$ is the external mode (barotropic) velocity interpolated from the external non-tidal ocean model, and U_{tide} denotes the barotropic velocity provided by the barotropic tidal model. The corrected boundary velocity value U_b at the time step t is then used for the momentum and tracer equations forward integration.

Equation (A4) is similar to the *Flather's* [1976] boundary condition for the regional tide simulation,

$$U_b = U_{no-tide} + U_{tide} \pm \sqrt{\frac{g}{H_b}} \cdot (\eta_{tide} + \eta_{no-tide} - \eta), \tag{A5}$$

where the sign of the correction term is positive for the western and southern, and negative for the eastern and northern open boundaries. The elevation relaxation parameter in equation (A5) is proportional to the free long gravity wave phase speed at each location instead of been a constant value. If we take the relaxation coefficient α_E in equation (A2) as

$$\alpha_E = \pm \sqrt{\frac{g}{H_b}} \frac{(H_b + \eta^{t+1}) \cdot dl_b \cdot \Delta t}{dS} \approx \sqrt{gH_b} \frac{\Delta t}{dn_b}, \tag{A6}$$

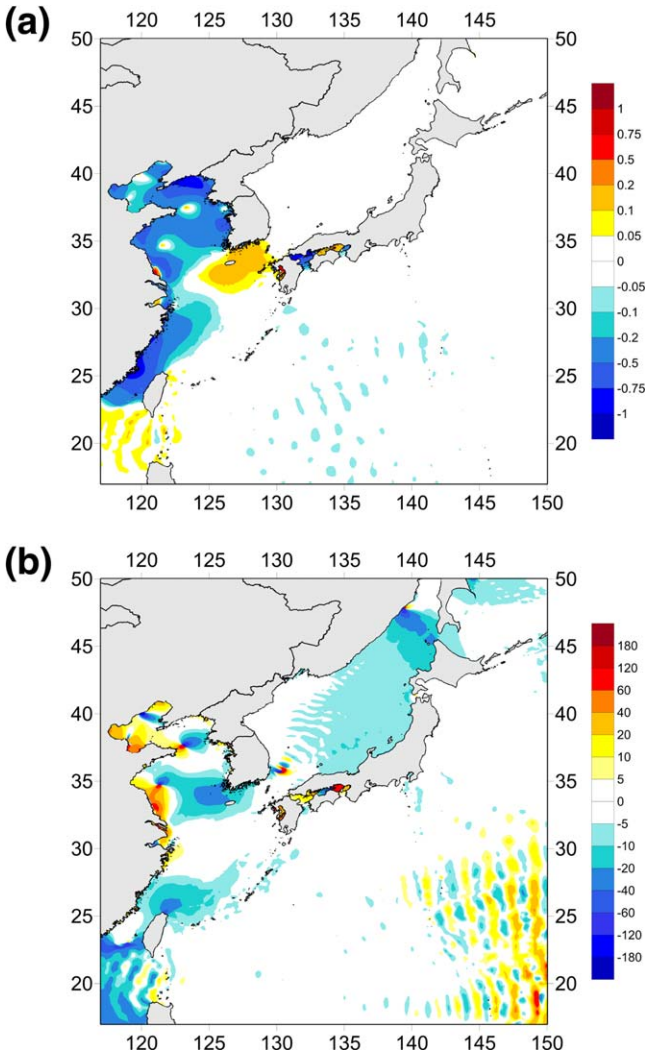

Figure A2. Difference of the (a) M_2 harmonic amplitude (in m) and (b) phase (in °) between JCOPE-T and OTIS models.

where dn_b is boundary cell linear size in normal to the open boundary direction, both the *Flather's* [1976] formulation (A5) and our approach (A2), (A3), (A4) become equivalent with possible differences only in numerical realization, like using forward predicted value of sea level for estimation of adjustment terms. In the described all numerical experiments, the boundary conditions: (A2), (A3), (A4), and (A6) are used.

Strong internal gravity waves are generated at topography slopes inside of the JCOPE-T model. Since the external model used for specifying boundary conditions (JCOPE2) does not include the tidal internal waves, we could expect that such waves must not be emitted or reflected from open boundaries into the interior of the nested model. We adopt a boundary sponge layer scheme for dumping of internal gravity waves coming to the open boundaries from the interior of the model domain. We apply a simple three points smoothing method to temperature, salinity, and baroclinic components of currents at the grids within six grid points inside from the open boundary with the smoothing weight decreasing linearly from it maximum value of 0.05 for the first model point near the open boundary to zero just outside of the sponge layer. Smoothing is done only in direction normal to open boundary that seems to be enough for not reflecting the internal waves at the boundary. We confirm that the sponge layer scheme effectively prevents propagation of the noisy disturbances generated near the open boundary toward the interior of the model region (not shown).

Appendix B: Validation of the Sea Level Variability in the Coastal Regions

To validate the simulated M_2 tide variations, we perform the harmonic analysis of both simulated and observed sea surface height anomaly data to extract four tidal constituents: O_1, K_1, M_2, and S_2. We analyze an along-track altimeter product of a satellite altimeter, Jason-2, with approximately 9.9 days interval for a 4.5 year period from July 2008 to January 2013. Note that the 4.5 year period is not long enough to separate the all eight constituents (e.g., O_1 and K_2) [*Schrama and Ray*, 1994] used as the major tidal driving force of JCOPE-T. The Jason-2 SSHA along-track product was produced by Ssalto/Duacs and distributed by Aviso, with support from the Centre National d'Etudes Spatiales. The data estimated from the Jason-2 altimeter are gridded on the JCOPE-T model grid for comparison.

Both of the satellite-observed and simulated M_2 amplitudes estimated on the model grids are averaged in square regions of 5° by 5° (Figures A1a and A1b). The spatial contrast of the simulated amplitude generally

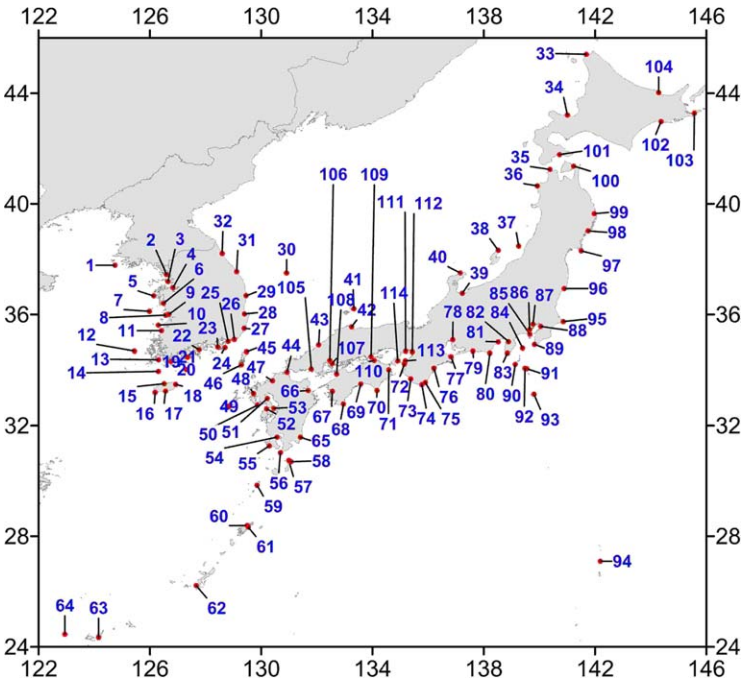

Figure A3. Location and reference numbers of the tide gauge stations used for the models validation.

agrees with the observation. Similar maps showing temporal correlation between observed and simulated M_2 amplitude and phase averaged in the square regions (Figures A1c and A1d) indicate that the model well simulates the M_2 tide variability as observed in the model domain except for some regions in the marginal seas such as Japan Sea, East China Sea, and Yellow Sea.

Tides in JCOPE-T model are introduced using the OTIS tidal model solution [*Egbert and Erofeeva*, 2002] through the forcing along open boundaries, and thus we compare the M_2 tide in JCOPE-T and OTIS models itself. For both JCOPE-T and OTIS models the harmonic analysis is performed for annual hourly reconstructed/simulated elevations from the base case experiment interpolated/extrapolated to the tidal gauge locations. Nearest grid point extrapolation is used for both models if interpolation is not possible. Figure A2a depicts the difference of M_2 tidal amplitudes in JCOPE-T minus OTIS. Around open boundaries and in deep sea, the difference is basically small and does not exceed 2–5 cm, but in marginal seas and coastal bays, it could be significant and exceeds 1 m. Distribution of the differences is also very irregular: close located could be areas of large positive and negative differences (near Chinese coast in the Yellow Sea, for example). Difference is also small over the M_2 tide amphidromic points that is especially clear in the Yellow and Bohai seas. It means that both models have an amphidromic points with the tidal amplitude going to zero in similar locations. Over the deep ocean, wave-like signal

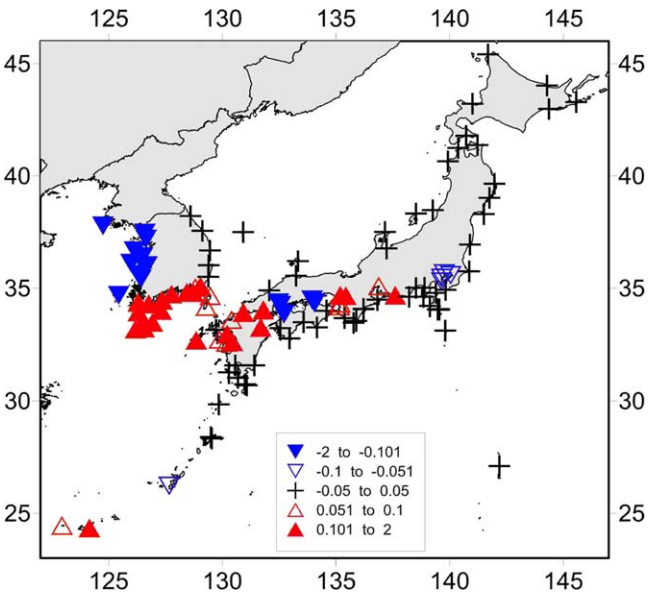

Figure A4. Distribution of absolute error of M_2 harmonic amplitude (in m) defined as difference in that between JCOPE-T and the tide gauge observation.

presents in the tide amplitudes difference that could be attributed to the manifestation of baroclinic tide on the sea surface discussed earlier in this paper. Phase difference of M_2 tidal constituents in both models is shown in Figure A2b, and its behavior has the similar features as has the amplitude differences distribution: generally large differences found in the marginal seas. Some specific is related with location of largest differences in phases near to the M_2 tide amphidromic points where, due to the small tide amplitude, the phase definition has large errors because it is related with division on approaching to zero amplitude value. Moderate phase difference up to 10° can be found in areas where the baroclinic tides are active. These areas include the spots analyzed in this work (Luzon Strait, Ogasawara Ridge, Tokara strait, and Izu Ridge) plus an area over the continental slope off the Tsushima strait with the beam of internal tidal waves propagating in to the Japan Sea [*Jeon et al.*, 2014].

For validation of the M_2 sea level variability reproduced by the JCOPE-T and OTIS models, we use the sea level observation data collected by Japan Coastal Guard (JCG), Japan Meteorological Agency (JMA), and Korean Hydrographic and Oceanographic Administration (KHOA) institutions. Data used for comparison with the model results passed a simple graphical quality control and suspicious spike data were removed. Location of used tidal gauges with the reference numbers is shown in Figure A3. Numbers given to stations are arranged so that these increase starting from the Korean stations in Yellow and East China Seas and moving with the land on the left along the Korean coast to Japan Sea, returning back from north to south along the Japanese coast of Japan Sea, and then going northward along the Japanese Pacific coast bypassing Seto Inland Sea. Stations in Seto Inland Sea are placed last as stations 105–114.

We compare the results of the two models with sea level observations at the tide gauge locations. To evaluate both amplitude and phase errors in this comparison, we use the absolute tidal harmonic error [*Matsumoto et al.*, 2000] as

$$Err = \sqrt{a_{obs}^2 + a_{\mathrm{mod}}^2 - 2 \cdot a_{obs} \cdot a_{\mathrm{mod}} \cdot (phase_{obs} - phase_{\mathrm{mod}})}, \tag{A7}$$

where a_{obs} and a_{mod} are amplitudes (in m), $phase_{obs}$ and $phase_{\mathrm{mod}}$ are phases (in radian) of observed and modeled M_2 tide, respectively. This value corresponds to the presentation of tidal harmonics as complex numbers or vectors. Average absolute error for M_2 tide at all analyzed 114 tidal gauges is 0.172 m for OTIS model and 0.168 for JCOPE-T that are very close to each other and are large values for some tidal gauges due to some errors that are not resolved by both models. However, to consider quality of the tide simulations compared to the observations, we examine distribution of JCOPE-T M_2 tide absolute error taken with the sign of M_2 amplitude error: it is positive if the model overestimates the observed amplitude of tide and negative if underestimates. Figure A4 plots five grades of JCOPE-T M_2 tide absolute error. Crosses indicate stations where relative absolute error does not exceed 5 cm. Such stations in majority are located in the

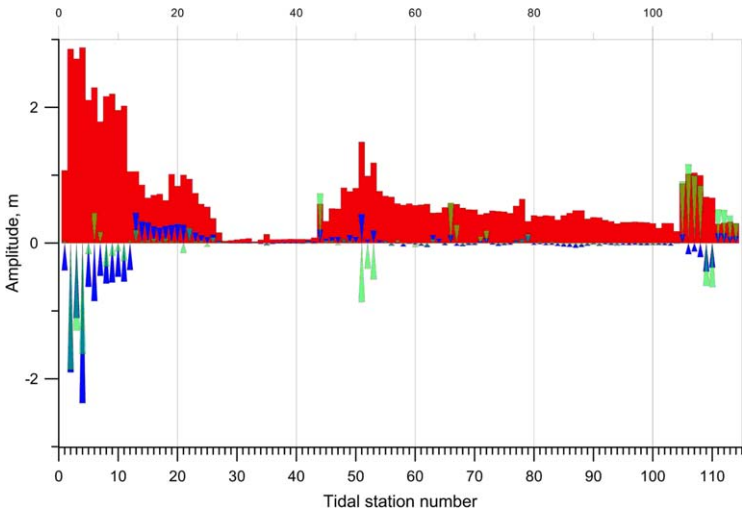

Figure A5. M_2 harmonic amplitude (in m) evaluated from the tide gauge observation (red bars). Horizontal axis denotes the reference number of the stations (see Figure A2 for locations). Blue cones denote the error defined by equation (A7) for M_2 harmonic (in m) with the sign of the M2 amplitude error of JCOPE-T model relative to the observation. Green cones denote the similar error of OTIS model.

Pacific and Japan Sea coast of Japan and in Ryukyu Islands south of Japan. Unfilled triangles indicate stations with absolute errors do not exceeding 10 cm and filled triangles denote other stations with relative difference larger 10 cm. Up-looking red triangles indicate stations where the simulated sea M_2 tide amplitude exceeds observed when down-looking blue triangles indicate stations where the model underestimates the observed M_2 tide. Overestimation by the model takes place at stations facing Tsushima Strait connecting East China Sea with Japan Sea. Along the Pacific coast of Japan large differences are found for number of stations that are located in coastal bays and in the Seto Inland Sea where this difference could be attributed to complicated coastal topography and coastline shape unresolved by the model with the horizontal resolution of 1/36° (approximately 3 km). Serious underestimation of M_2 barotropic tide takes place for stations along the western coast of Korean Peninsula. Majority of tidal gauges there are located in shallow bays with very complicated topography that makes it difficult for reproducing tidal variability there with the 3 km resolution as we already mentioned for small semienclosed seas of Japan.

To check possible model dependence, we plot in Figure A5 the amplitude of M_2 sea level tide harmonic at tidal gauges as red bars, and signed absolute error of M_2 JCOPE-T (blue cones) and OTIS (green cones) sea level tide relative to the observations. For first 22 stations located along the Korean coast, JCOPE-T has mainly larger errors except for some stations where errors are extremely large and which are unresolved by both OTIS and JCOPE-T. But basically for all stations from No. 27 and forward JCOPE-T errors are very small and for many Japanese coastal stations clearly smaller compared with these for the OTIS data. Especially large differences are for last stations located in Seto Inland Sea that is very badly resolved by the 1/12° OTIS model. We conclude that large errors in reproducibility of tidal sea level variability along the western and southern coast of Korea is a difficult task not for our model only, but even for the specialized tide simulation model with the assimilation of the tidal data like OTIS.

As shown in the JCOPE-T simulation results, we have both cases of overestimation and underestimation of sea level variability compared to that observed on the tidal gauges. The problem of overestimated tide amplitude was reported by *Arbic et al.* [2010] for their simulation with the global baroclinic tide model. In the baroclinic tide models, barotropic tide energy has to be transferred to internal tides. Breaking of internal waves finally removes the excess of energy from the model. Although our model JCOPE-T has the horizontal resolution of 1/36° that is finer than 1/12.5° for the HYCOM model of *Arbic et al.'s* [2010] results, JCOPE-T still does not completely resolve the processes of generation and breaking of higher vertical mode internal waves. But this explanation does not cover the cases of underestimated sea level variability for group of tidal gauges at the western coast of Korean Peninsula, implying that the horizontal resolution of 3 km is still too coarse to resolve the tidal variability affected by the complicated bottom and coastal topography in this region, and/or the dissipation of the tide is overestimated there.

Acknowledgments
This work is part of the Japan Coastal Ocean Predictability Experiment (JCOPE) promoted by the Japan Agency for Marine-Earth Science and Technology (JAMSTEC). The altimeter products were produced by Ssalto/Duacs and distributed by Aviso with support from CNES (http://www.aviso.oceanobs.com/duacs/). The sea level observation data collected by Japan Coastal Guard (JCG) and Japan Meteorological Agency (JMA) are available from http://www1.kaiho.mlit.go.jp/KANKYO/TIDE/real_time_tide/sel/ and the data collected by Korean Hydrographic and Oceanographic Administration (KHOA) institutions are available from http://www.khoa.go.kr/. The Oregon State University Tidal Inversion Software (OTIS) model data are available from http://volkov.oce.orst.edu/tides/. The simulation data for this paper are available from the authors (http://www.jamstec.go.jp/jcope/vwp/). Computation codes for the tidal harmonic and energy analyses were kindly provided by Takashi Kagimoto and Hideyuki Kawajiri. We thank two anonymous reviewers for their suggestive and constructive comments on the earlier versions of the manuscript. KI and YM are supported by JSPS KAKENHI (26400468).

References

Arbic, B. K., A. J. Wallcraft, and E. J Metzger (2010), Concurrent simulation of the eddying general circulation and tides in a global ocean model, *Ocean Modell.*, *32*, 175–187.
Arbic, B. K., J. G. Richman, J. F. Shriver, P. G. Timko, E. J. Metzger, and A. J. Wallcraft (2012), Global modeling of internal tides within an eddying ocean general circulation model, *Oceanography*, *25*, 20–29.
Baines, P. G. (1973), The generation of internal tides by flat-bump topography, *Deep Sea Res. Oceanogr. Abstr.*, *20*, 179–205.
Berntsen, J., and L.-Y. Oey (2010), Estimation of the internal pressure gradient in σ-coordinate ocean models: Comparison of second-, fourth-, and sixth-order schemes, *Ocean Dyn.*, *60*, 317–330.
Boris, J. P., and D. L. Book (1973), Flux-corrected transport I: SHASTA, a fluid transport algorithm that works, *J. Comput. Phys.*, *11*, 38–69.
Chavanne, C., P. Flament, D. Luther, and K.-W. Gurgel (2010), The surface expression of semidiurnal internal tides near a strong source at Hawaii. Part II: Interactions with mesoscale currents, *J. Phys. Oceanogr.*, *40*, 1180–1200.
Conkright, M. E., R. A. Locarnini, H. E. Garcia, T. D. O'Brien, T. P. Boyer, C. Stephens, and J. I. Antonov (2002), *World Ocean Atlas 2001: Objective Analyses, Data Statistics, and Figures* [CD-ROM], 17 pp., Natl. Oceanogr. Data Cent., Silver Spring, Md.
Cox, C. S., and H. Sandstrom (1962), Coupling of internal and surface waves in water of variable depth, *J. Oceanogr. Soc. Jpn.*, 20th Anniv. Vol., 499–513.
Egbert, G. D., and S. Y. Erofeeva (2002), Efficient inverse modeling of barotropic ocean tides, *J. Atmos. Oceanic Technol.*, *19*(2), 183–204, doi: 10.1175/1520-0426(2002)019<0183:EIMOBO>2.0.CO;2.
Egbert, G. D., A. F. Bennet, and M. G. G. Foreman (1994), TOPEX/POSEIDON tides estimated using a global inverse model, *J. Geophys. Res.*, *99*(C12), 24,821–24,852.
Eich, M. L., M. A. Merriefield, and M. H. Alford (2004), Structure and variability of semidiurnal internal tides in Mamala Bay, Hawaii, *J. Geophys. Res.*, *109*, C05010, doi:10.1029/2003JC002049.
Emery, W. J., W. G. Lee, and L. Magaard (1984), Geographical and seasonal distributions of Brunt-Vaisala frequency and Rossby radii in the North Pacific and North Atlantic, *J. Phys. Oceanogr.*, *14*, 294–317.
Flather, R. A. (1976), A tidal model of the northwest European continental shelf, *Mem. Soc. R. Sci. Liege*, *6*, 141–164.
Guo, X., and T. Yanagi (1998), Three-dimensional structure of tidal current in the East China Sea and the Yellow Sea, *J. Oceanogr.*, *54*, 651–668.

Guo, X., H. Hukuda, Y. Miyazawa, and T. Yamagata (2003), A triply nested ocean model simulating the Kuroshio—Roles of horizontal resolution on JEBAR, *J. Phys. Oceanogr.*, *33*, 146–169.
Jan, S., C.-S. Chen, J. Wang, and M.-D. Chiou (2012), Generation and propagation of baroclinic tides modified by the Kuroshio in the Luzon Strait, *J. Geophys. Res.*, *117*, C02019, doi:10.1029/2011JC007229.
Jeon, C., J.-H. Park, S. M. Varlamov, J.-H. Yoon, Y. H. Kim, S. Seo, Y.-G. Park, H. S. Min, J. H. Lee, and C.-H. Kim (2014), Seasonal variation of semidiurnal internal tides in the East/Japan Sea, *J. Geophys. Res. Oceans*, *119*, 2843–2859, doi:10.1002/2014JC009864.
Kantha, L. H., and C. A. Clayson (2000), *Numerical Models of Oceans and Oceanic Processes, Int. Geophys. Ser.*, vol. 66, 940 pp., Academic Press, San Diego, Calif.
Kantha, L. H., and C. C. Tierney (1997), Global baroclinic tide, *Prog. Oceanogr.*, *40*, 163–178.
Kartadikaria, A. R., Y. Miyazawa, S. M. Varlamov, and K. Nadaoka (2011), Ocean circulation for the Indonesian seas driven by tides and atmospheric forcings: Comparison to observational data, *J. Geophys. Res.*, *116*, C09009, doi:10.1029/2011JC007196.
Kerry, C. G., B. S. Powell, and G. S. Carter (2013), Effects of remote generation sites on model estimates of M_2 internal tides in the Philippine Sea, *J. Phys. Oceanogr.*, *43*, 187–204.
Kerry, C. G., B. S. Powell, and G. S. Carter (2014), The impact of subtidal circulation on internal tide generation and propagation in the Philippine Sea, *J. Phys. Oceanogr.*, *44*, 1386–1405.
Kouketsu, S., H. Tomita, E. Oka, S. Hosoda, T. Kobayashi, and K. Sato (2012), The role of meso-scale eddies in mixed layer deepening and mode water formation in the western North Pacific, *J. Oceanogr.*, *68*, 63–77.
Kutzbach, J. (1967), Empirical eigenvectors of sea level pressure, surface temperature, and precipitation complexes over North America, *J. Appl. Meteorol.*, *6*, 791–802.
Li, Y., Z. Gao, D. H. Lenschow, F. Chen (2010), An improved approach for parameterizing surface-layer turbulent transfer coefficients in numerical models, *Boundary Layer Meteorol.*, *137*, 153–165.
Lorenzo, E. D., W. R. Young, and S. L. Smith (2006), Numerical and analytical estimates of M_2 tidal conversion at steep oceanic ridges, *J. Phys. Oceanogr.*, *36*, 1072–1084.
Matsumoto, K., T. Takanezawa, and M. Ooe (2000), Ocean tide models developed by assimilating TOPEX/POSEIDON altimeter data into hydrodynamical model: A global model and a regional model around Japan, *J. Oceanogr.*, *56*, 567–581.
McCalpin, J. D. (1994), A comparison of second-order and fourth-order pressure gradient algorithms in a sigma coordinate ocean model, *Int. J. Numer. Methods Fluids*, *18*, 361–383.
Mellor, G. (2002), *Users Guide for a Three-Dimensional, Primitive Equation, Numerical Ocean Model*. [Available at http://www.ccpo.odu.edu/POMWEB/UG.10-2002.pdf.]
Mellor, G., and A. F. Blumberg (2004), Wave breaking and ocean surface layer thermal response, *J. Phys. Oceanogr.*, *34*, 693–698.
Mellor, G., S. Hakkinen, T. Ezer, and R. Patchen (2002), A generalization of a sigma coordinate ocean model and an intercomparison of model vertical grids, in *Ocean Forecasting: Conceptual Basis and Applications*, edited by N. Pinardi and J. D. Woods, pp. 55–72, Springer, New York.
Mellor, G. L., and T. Yamada (1982), Development of a turbulence closure model for geophysical fluid problems, *Rev. Geophys. Space Phys.*, *20*, 851–875.
Ministry of Land, Infrastructure, Transport, and Tourism (2002), Annual record of river discharges in Japan. [Available at http://www.stat.go.jp/data/chouki/zuhyou/01-05.xls.]
Miyazawa, Y., R. Zhang, X. Guo, H. Tamura, D. Ambe, J.-S. Lee, A. Okuno, H. Yoshinari, T. Setou, and K. Komatsu (2009), Water mass variability in the western North Pacific detected in a 15-year eddy resolving ocean reanalysis, *J. Oceanogr.*, *65*, 737–756.
Miyazawa, Y., Y. Masumoto, S. M. Varlamov, and T. Miyama (2012), Transport simulation of the radionuclide from the shelf to open ocean around Fukushima, *Cont. Shelf Res.*, *50–51*, 16–29.
Miyazawa, Y., Y. Masumoto, S. M. Varlamov, T. Miyama, M. Takigawa, M. Honda, and T. Saino (2013), Inverse estimation of source parameters of oceanic radioactivity dispersion models associated with the Fukushima accident, *Biogeosciences*, *10*, 2349–2363.
Munk, W. H., and C. Wunsh (1998), Abyssal recipes, II: Energetics of tidal and wind mixing, *Deep Sea Res., Part I*, *45*, 1977–2010.
Niwa, Y., and T. Hibiya (2001), Numerical study of the spatial distribution of the M_2 internal tide in the Pacific Ocean, *J. Geophys. Res.*, *106*(C10), 22,441–22,449.
Niwa, Y., and T. Hibiya (2004), Three-dimensional numerical simulation of M_2 internal tides in the East China Sea, *J. Geophys. Res.*, *109*, C04027, doi:10.1029/2003JC001923.
Niwa, Y., and T. Hibiya (2011), Estimation of baroclinic tide energy available for deep ocean mixing based on three-dimensional global numerical simulations, *J. Oceanogr.*, *67*, 493–502.
Osborne, J. J., A. L. Kurapov, G. D. Egbert, and P. M. Kosro (2011), Spatial and temporal variability of the M_2 internal tide generation and propagation on the Oregon Shelf, *J. Phys. Oceanogr.*, *41*, 2037–2062.
Pascual, A., Y. Faugere, G. Larnicol, and P.-Y. Le Traon (2006), Improved description of the ocean mesoscale variability by combining four satellite altimeters, *Geophys. Res. Lett.*, *33*, L02611, doi:10.1029/2005GL024633.
Pereira, A. F., B. M. Castro, L. Calado, and I. C. A. da Silveira (2007), Numerical simulation of M_2 internal tides in the South Brazil Bight and their interaction with the Brazil Current, *J. Geophys. Res.*, *112*, C04009, doi:10.1029/2006JC003673.
Petrelis, F., S. L. Smith, and W. R. Young (2006), Tidal conversion at a submarine ridge, *J. Phys. Oceanogr.*, *36*, 1053–1071.
Qiu, B., S. Chen, and G. S. Carter (2012), Time-varying parametric subharmonic instability from repeat CTD surveys in the northwestern Pacific Ocean, *J. Geophys. Res.*, *117*, C09012, doi:10.1029/2012JC007882.
Qu, T., H. Mitsudera, and B. Qiu (2001), A climatological view of the Kuroshio/Oyashio system east of Japan, *J. Phys. Oceanogr.*, *31*, 2575–2589.
Ray, R. D., and G. T. Mitchum (1996), Surface manifestation of internal tides generated near Hawaii, *Geophys. Res. Lett.*, *23*(16), 2101–2104.
Schrama, E. J. O., and R. D. Ray (1994), A preliminary tidal analysis of TOPEX/POSEIDON altimetry, *J. Geophys. Res.*, *99*(C12), 24,799–24,808.
Sheu, W.-J., C.-R. Wu, and L.-Y. Oey (2010), Blocking and westward passage of eddies in the Luzon Strait, *Deep Sea Res., Part II*, *57*, 1783–1791.
Smagorinsky, J. (1963), General circulation experiments with the primitive equations. I. The basic experiment, *Mon. Weather Rev.*, *91*, 99–164.
Waldron, K. M., J. Paegle, and J. D. Horel (1996), Sensitivity of a spectrally filtered and nudged limited-area model to outer model options, *Mon. Weather Rev.*, *124*, 529–547.
Wang, Q., X. Guo, and H. Takeoka (2008), Seasonal variations of the river plume in the Bohai sea: A model study, *J. Geophys. Res.*, *113*, C08046, doi:10.1029/2007JC004555.
Wunsch, C. H. (1975), Internal tide in the ocean, *Rev. Geophys. Space Phys.*, *13*, 167–182.
Zilverman, N. V., M. A. Merrifield, G. S. Carter, D. S. Luther, M. D. Levine, and T. J. Boyd (2011), Incoherent nature of M_2 internal tides at the Hawaiian Ridge, *J. Phys. Oceanogr.*, *41*, 2021–2036.